

# 7

## *Phase-Shifting Systems and Phase-Shifting Analysis*

Qingying Hu

### CONTENTS

7.1	Introduction.....	288
7.2	Phase-Shifting System and Its Benefits .....	288
7.2.1	Fringe Patterns .....	288
7.2.1.1	Interference Fringe Pattern.....	289
7.2.1.2	Moiré Pattern .....	289
7.2.1.3	Fringe Projection with a Physical Grating.....	290
7.2.1.4	Digital Fringe Projection.....	290
7.2.1.5	Other Special Fringe Patterns .....	291
7.2.2	Fringe Pattern Analysis.....	291
7.2.2.1	Contour Analysis .....	291
7.2.2.2	Phase-Shifting Analysis.....	292
7.2.2.3	Benefits of Phase-Shifting Analysis .....	295
7.2.3	Phase-Shifting Systems.....	296
7.2.3.1	Physical Phase-Shifting System .....	297
7.2.3.2	Digital Phase-Shifting System.....	297
7.2.3.3	Simultaneous Phase-Shifting Techniques.....	298
7.3	Phase-Shifting Algorithms for Phase Wrapping .....	299
7.3.1	General Phase-Shifting Algorithm .....	299
7.3.2	Common Phase-Shifting Algorithms .....	300
7.3.2.1	Three-Step Phase-Shifting Algorithm .....	300
7.3.2.2	Double Three-Step Phase-Shifting Algorithm .....	300
7.3.2.3	Four-Step Phase-Shifting Algorithm .....	301
7.3.2.4	Carré Phase-Shifting Algorithm.....	302
7.3.2.5	Five-Step Phase-Shifting Algorithm (Hariharan Algorithm) .....	303
7.3.2.6	Phase-Shifting Algorithms with More Than Five Steps .....	304
7.3.2.7	Spatial Carrier Phase-Shifting Algorithms .....	304
7.3.3	Selection of Phase-Shifting Algorithms .....	304
7.4	Phase-Shifting System Modeling and Calibration.....	305
7.4.1	Modeling of Phase-Shifting Measurement System .....	305
7.4.1.1	Unwrapped Phase Map and Absolute Phase Map.....	306
7.4.1.2	Linear Model for Flat Surface Measurement .....	307
7.4.1.3	Partially Linear Model for Flat Surface Measurement .....	308
7.4.1.4	Nonlinear Model for Complex Shape .....	309
7.4.2	Phase-Shifting System Calibration.....	310
7.4.2.1	Camera Calibration.....	311
7.4.2.2	Projector Calibration.....	315

7.5	Error Analysis and Compensation for Phase-Shifting Systems .....	318
7.5.1	Error Sources and Adjustment in the Phase-Shifting System .....	319
7.5.1.1	Phase-Shifting Error .....	319
7.5.1.2	Nonlinearity Error in the Detector/Projector .....	320
7.5.1.3	Modeling and Calibration Error .....	321
7.5.1.4	Imbalance Error for Color Fringe Projections.....	321
7.5.1.5	Quantization Error.....	321
7.5.1.6	Error and Noise from Environment.....	321
7.5.2	Nonlinearity Compensation with the Projector Gamma $\gamma$ .....	322
7.5.2.1	Gamma Correction with the Response Curve.....	322
7.5.2.2	Gamma Correction with a One-Parameter Gamma Model .....	324
7.5.3	Phase Error Compensation.....	325
7.5.4	Coordinate Compensation.....	326
7.5.4.1	Coordinate Error Map .....	326
7.5.4.2	Coordinate Error Compensation .....	327
7.6	Summary.....	328
	References.....	328

---

## 7.1 Introduction

Phase-shifting surface profile measurement is a very important branch in optical metrology. When compared with other surface measurement techniques, it has many unique features such as varieties of configurations, high resolution, high accuracy, good repeatability, fast measurement speed, and superior surface finish tolerance. Especially in the past several decades, with the help of digital image devices and dedicated computer software, phase-shifting images were automatically processed at high speed over a full field of view (FOV), further enabling superfast 3D measurement without scanning. This chapter covers most of the aspects related to phase-shifting systems, including system configurations, phase-shifting algorithms, modeling and calibration of phase-shifting systems, and error analysis and compensation for accuracy improvement.

---

## 7.2 Phase-Shifting System and Its Benefits

Depending on how a fringe pattern is generated and how it is shifted, various phase-shifting configurations are available for use in optical metrology, aiming at different applications.

### 7.2.1 Fringe Patterns

A fringe pattern is a periodic grayscale pattern with alternative dark and bright areas. Based on pattern generation principles, the most common fringe pattern can be classified into three categories: interference pattern, moiré pattern, and projected pattern.

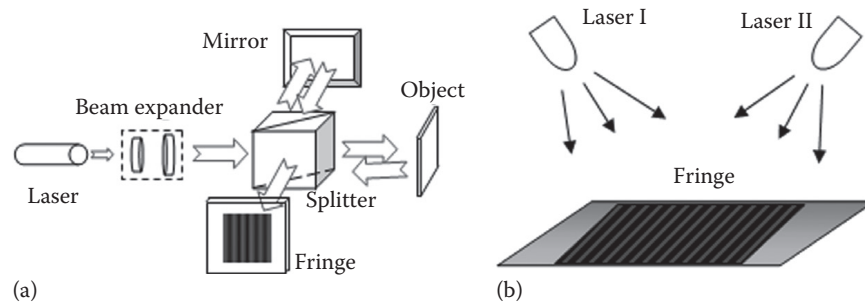


**FIGURE 7.1**  
Interferometers: (a) Michelson interferometer and (b) AFI.

### 7.2.1.1 Interference Fringe Pattern

An interference pattern is well known in optical interferometers. When two coherent light beams with common polarization superpose in an area, at each point, the resulting light intensity, shown as grayscale in a camera, depends on the optical path difference (OPD) between these two light sources reaching this point. The OPD results in phase difference at a certain point, destructive or constructive, forming periodic pattern on the object surface. A good example is the famous Young's experiment in optics.<sup>1</sup>

In optical metrology, the two slots in Young's experiment are usually replaced by a splitter, either polarized or nonpolarized, to generate two wave fronts: one is a measurement wave front that is modulated by the geometric variation of the surface, and the other is a reference wave front under good control. When these two wave fronts superpose, the difference between them is revealed in an interference fringe pattern. A typical Michelson interferometer is shown in Figure 7.1a. Adjusting the tilting angle of the reference mirror will change the pitch of the fringe pattern. This interferometer has very high resolution, up to hundredth of wavelength, but the FOV is usually limited because the light beam diameter after expansion has to be slightly larger than the FOV so as to conform to the related components. For large FOV measurements, the system will be too large and too costly.

To measure a large area with a small instrument footprint, a technique called Accordion Fringe Interferometry (AFI) was developed at MIT's Lincoln Laboratory in 1990s,<sup>2</sup> as shown in Figure 7.1b. AFI uses two-point lasers to illuminate the target divergently and a camera to record the interference fringe pattern that is modulated by the surface geometry of the sample under measurement. It also provides excellent accuracy performance with a large FOV but small footprint. Because the fringe pattern results from laser interference, the depth of focus for the fringe projection unit is infinite.

### 7.2.1.2 Moiré Pattern

A shadow moiré pattern looks like an interference pattern, but its geometric interference principle is very different.<sup>3-5</sup> Figure 7.2a shows a representative shadow moiré fringe image. It is generated by covering the measurement area with a physical grating while illuminating and viewing the area from an opposite direction, as shown in Figure 7.2b. When light passes through the grating at a tilted angle, a shadow of the grating will be generated on the sample surface. When this shadow is observed at a tilted angle from the opposite direction to the light source, a moiré pattern can be seen that represents the topology of the surface with the peak/valley rings representing the same height relative to the physical grating.

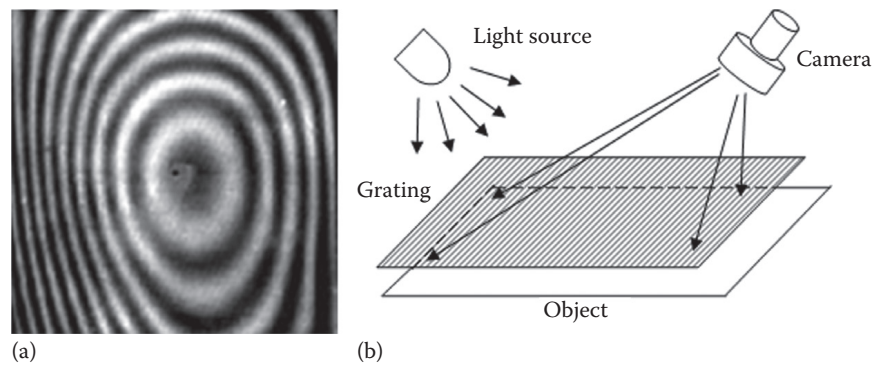


**FIGURE 7.2**  
Shadow moiré: (a) moiré pattern and (b) setup.

### 7.2.1.3 Fringe Projection with a Physical Grating

When a transmission grating with a sinusoidal transmission profile such as holographic gratings is placed between a light source and a projection lens, the projected fringe pattern will also have a sinusoidal intensity profile, as shown in Figure 7.3a.<sup>6</sup> If a straight-line grating with a nonsinusoidal profile such as a ruled grating is used, the projection lens is usually defocused slightly so that a pseudo-sinusoidal pattern can be obtained. Figure 7.3b shows a projected fringe on an edge break.

Another technique called projection moiré requires a second physical grating to be placed before the camera lens.<sup>7</sup> The second grating can have a different pitch than that of the first grating used for fringe projection. In this configuration, a traditional moiré pattern will be captured in the imaging system. This technique is out of focus of this chapter but has been covered in Chapter 8.

### 7.2.1.4 Digital Fringe Projection

In digital fringe projection,<sup>8-10</sup> the fringe pattern can be generated with theoretically any intensity profile using computer software and projected to the object surface through an

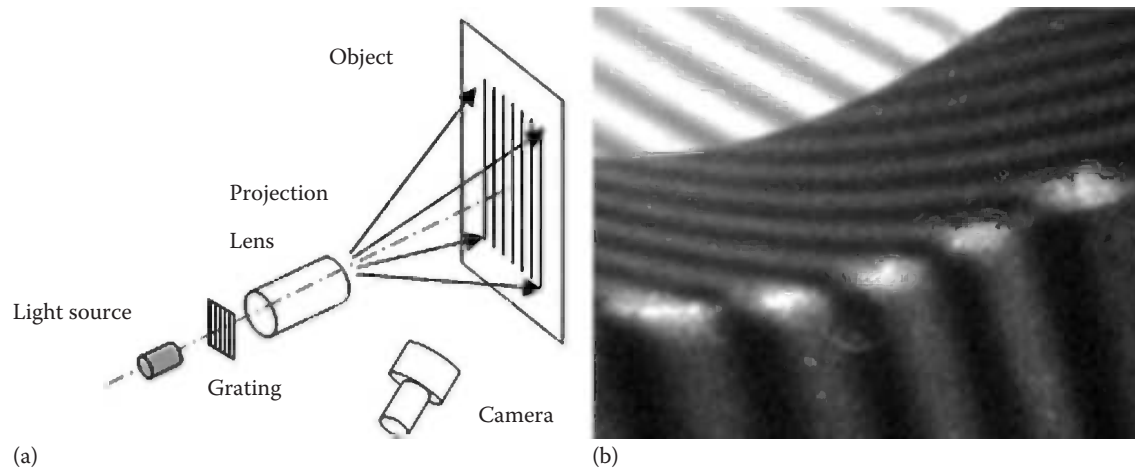


**FIGURE 7.3**  
Projection moiré: (a) setup and (b) pattern.

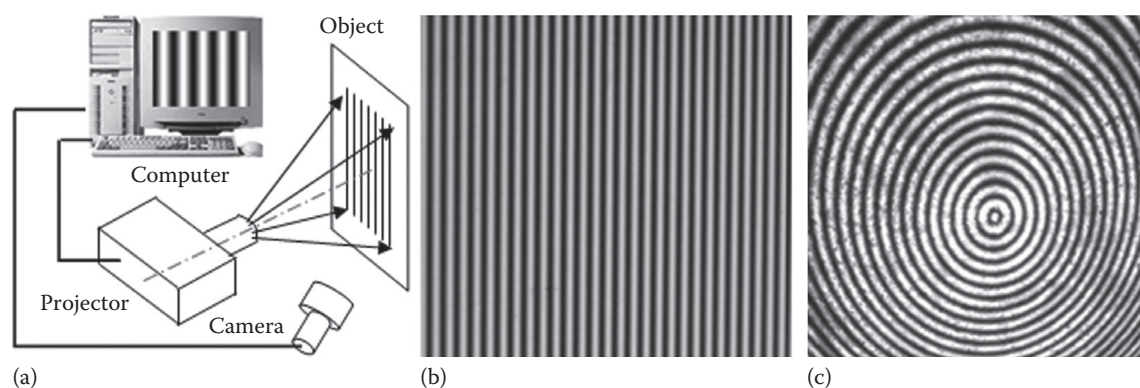


**FIGURE 7.4**  
Digital fringe projection: (a) setup, (b) straight fringe pattern, and (c) circular fringe pattern.

off-the-shelf digital projector such as liquid crystal device (LCD), digital mirror device (DMD), and liquid crystal on silicon (LCOS) projectors. This provides a low-cost and flexible solution for fringe projection techniques. Figure 7.4 shows the typical set up and two projected fringe patterns.

### 7.2.1.5 Other Special Fringe Patterns

All fringe patterns discussed so far have sinusoidal or pseudo-sinusoidal intensity profiles. Sometimes, other special fringe patterns are also used for a specific purpose such as speed and simplicity considerations. These patterns include the trapezoidal pattern,<sup>11–13</sup> sawtooth,<sup>14</sup> and slope profile. Because this chapter focuses on traditional phase-shifting techniques related to sinusoidal patterns, these special patterns and related algorithms are not investigated further. Interested readers can find details in the corresponding references.

## 7.2.2 Fringe Pattern Analysis

### 7.2.2.1 Contour Analysis

To extract the geometric information in the fringe pattern, an appropriate analysis methodology has to be used. To better understand the challenges, it is necessary to take a look at the intensity profile of the captured fringe pattern image. Without losing generality, a representative cross section near the middle horizontal line of the fringe pattern depicted in Figure 7.2 is taken as an example shown in Figure 7.5.

Before the phase-shifting technique was invented, the only way to investigate the fringe pattern image was to count the peak and/or valley and follow the contour curve along the peaks and valleys,<sup>3</sup> as demonstrated in Figure 7.6. The calibration process was to find the factor that converted the peak/valley into the height dimension and was used to estimate the height variation over the FOV. The denser these fringes are, the steeper the slope magnitude is of the surface area. The resolution and accuracy of this analysis method was very low, and there is no way to identify the direction of the slopes from a single image without introducing a known tilt to the part, creating a bias fringe larger than any other expected slope. That is, by tilting the part, all slopes are made to be perturbations to that slope. The requirement for a bias greatly limits the use of such systems for measuring real parts.

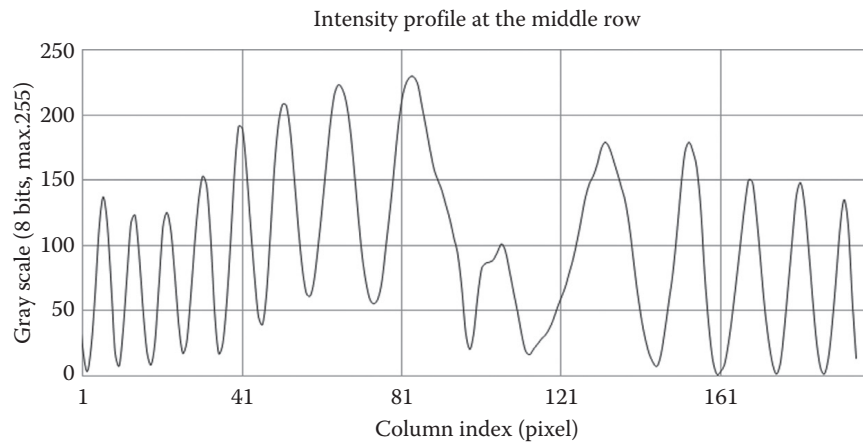


**FIGURE 7.5**  
Intensity profile of the middle horizontal cross section in the moiré fringe.

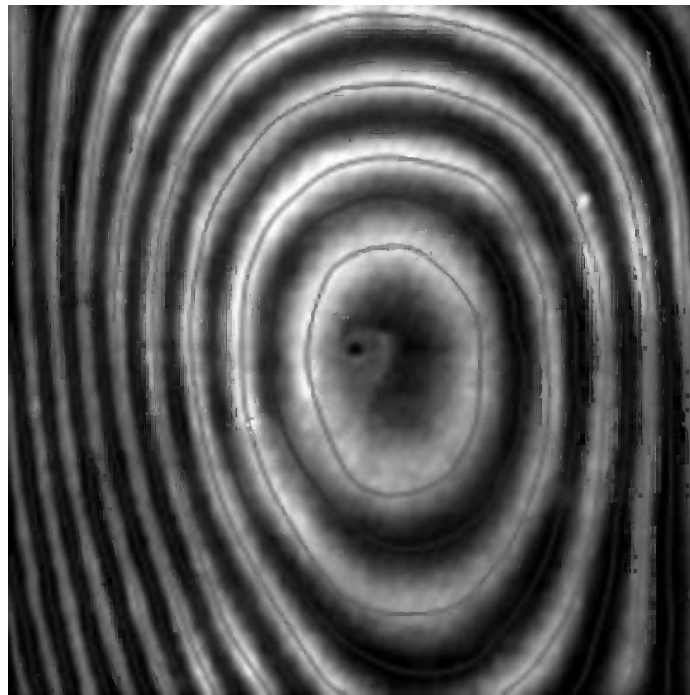


**FIGURE 7.6**  
Contour showing peak (bright bands) and valley (dark bands).

### 7.2.2.2 Phase-Shifting Analysis

In the 1970s, thanks to the invention of digital cameras and computers, digital image analysis started to be used in optical metrology, and the phase-measuring methods became a reality that greatly improved the resolution, accuracy, speed, and repeatability of interferometers and moiré technology.<sup>15</sup> Over the years, various phase-measuring methods have been developed, with the phase-shifting method being the technique most widely used.<sup>16,17</sup>

An entire phase-shifting analysis process is demonstrated in Figure 7.7 using a three-step phase-shifting algorithm. In Figure 7.7, the three images in the top row are captured three fringe images of a master model with a  $120^\circ$  phase shift. The intensities of the three phase-shifted images at point  $(x, y)$  can be written as

$$I_1(x, y) = I'(x, y) + I''(x, y) \cos \left[ \phi(x, y) - \frac{2\pi}{3} \right] = I'(x, y) \left\{ 1 + \gamma(x, y) \cos \left[ \phi(x, y) - \frac{2\pi}{3} \right] \right\} \quad (7.1)$$

$$I_2(x, y) = I'(x, y) + I''(x, y) \cos [\phi(x, y)] = I'(x, y) \left\{ 1 + \gamma(x, y) \cos [\phi(x, y)] \right\} \quad (7.2)$$

$$I_3(x, y) = I'(x, y) + I''(x, y) \cos \left[ \phi(x, y) + \frac{2\pi}{3} \right] = I'(x, y) \left\{ 1 + \gamma(x, y) \cos \left[ \phi(x, y) + \frac{2\pi}{3} \right] \right\} \quad (7.3)$$

where

$I'(x, y)$  is the average intensity

$I''(x, y)$  is the intensity modulation

$\phi(x, y)$  is the phase to be determined

By solving the earlier equations, phase  $\phi(x, y)$  and image contrast  $\gamma(x, y)$  can be obtained as

$$\phi(i, j) = \tan^{-1} \left( \sqrt{3} \frac{I_1 - I_3}{2I_2 - I_1 - I_3} \right) \quad (7.4)$$

$$\gamma(i, j) = \frac{I''(x, y)}{I'(x, y)} = \frac{\left[ (I_3 - I_2)^2 + (2I_1 - I_2 - I_3)^2 \right]^{1/2}}{I_2 + I_3} \quad (7.5)$$

This wrapped phase map includes the modulo  $2\pi$  discontinuity, as shown in Figure 7.8. The continuous phase map  $\Phi(i, j)$  can be obtained by use of a phase-unwrapping algorithm, as shown in Figure 7.9. How to implement a fast and robust phase-unwrapping process in computer software programming for a complex irregular 2D geometry with various slopes and discontinuity, such as holes, requires one to have both programming skills and an understanding of the phase-unwrapping principle. This is a complex issue that will require an entire book to discuss.<sup>18</sup>

Because the values of the unwrapped phase depend on the starting point of the unwrapping process, the obtained phase map is a relative phase map and cannot be used directly to represent the surface geometry although it contains the geometric information. For flat surfaces, the phase map can be either subtracted from a reference phase map or brought down to reveal the defects or qualitative geometric features, as shown in Figure 7.10. But for a complex geometry shape or quantitative dimension comparison with geometric tolerance, the difference among the actual surface geometry and phase map is obvious, as shown in the bottom row of Figure 7.7. However, when used with the appropriate model and phase-to-coordinate conversion algorithm,<sup>19,20</sup> an accurate 3D shape can be reconstructed from the wrapped phase map, as shown in the bottom-right picture of Figure 7.7.

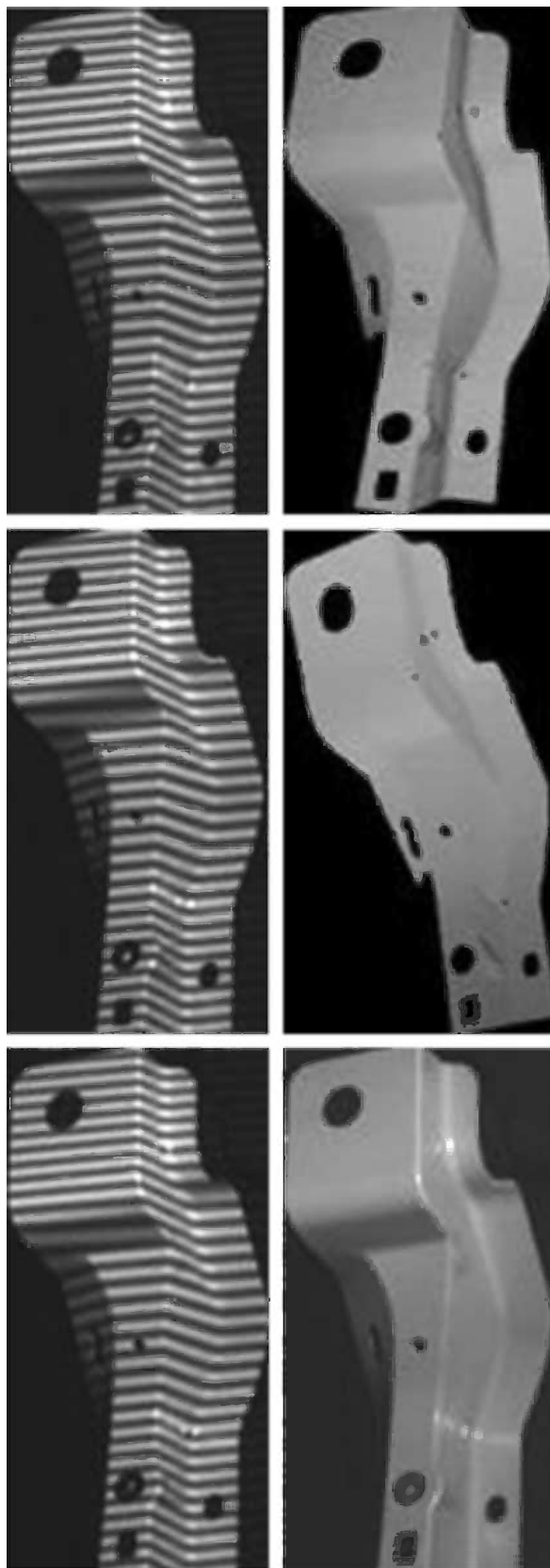


**FIGURE 7.7**  
Phase-shifting fringe analysis process.

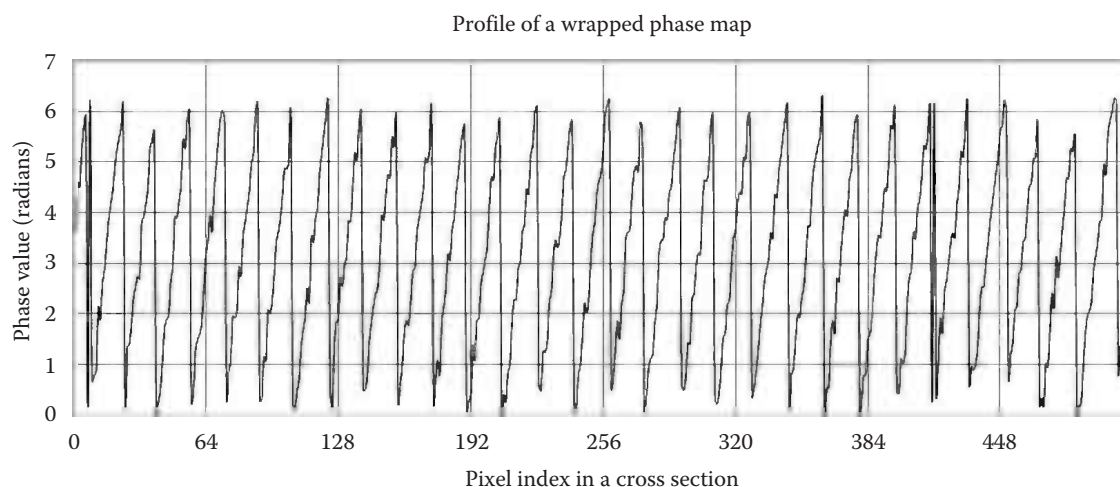


**FIGURE 7.8**  
Profile of a wrapped phase map with  $2\pi$  discontinuity.

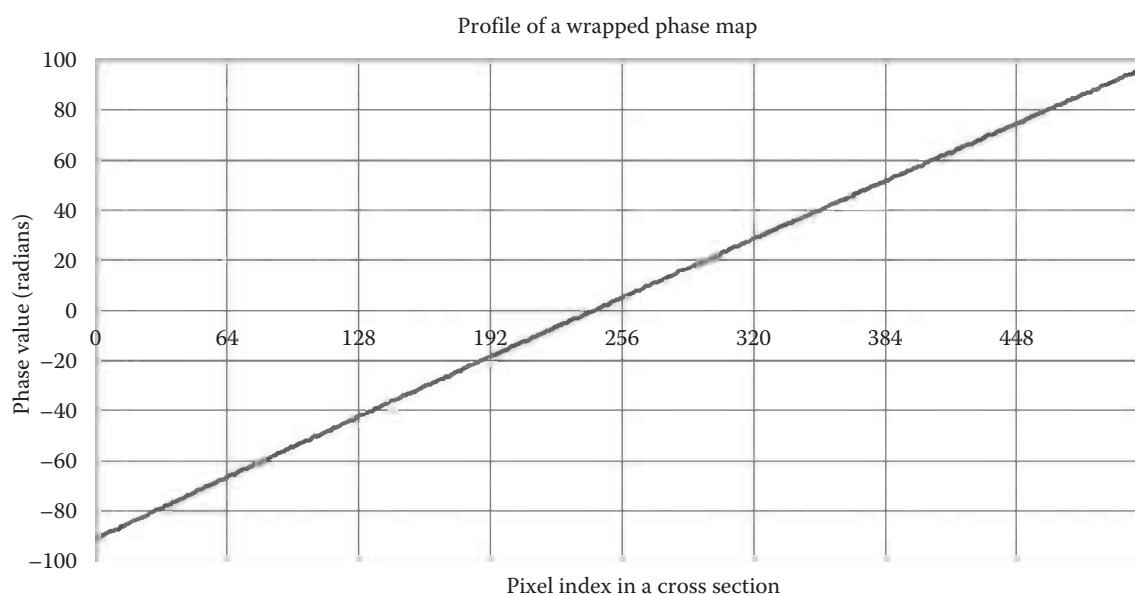


**FIGURE 7.9**  
Profile of an unwrapped phase map without  $2\pi$  discontinuity.

### 7.2.2.3 Benefits of Phase-Shifting Analysis

The phase-shifting analysis enables full-field analysis in areas because it provides geometric information for all sampled points between intensity peak/valleys. The obtained phase map provides directional information such as the positive or negative slopes and convex or concave local curvatures, along both lateral and vertical directions.

The phase-shifting analysis obtains phase information from image contrast, not intensity changes from peak to valley, thus enabling much higher accuracy and making the analysis tolerant to various surface finishes, including shiny surfaces on some parts. Figure 7.11 shows how the phase-shifting technique can be used to obtain dimensional

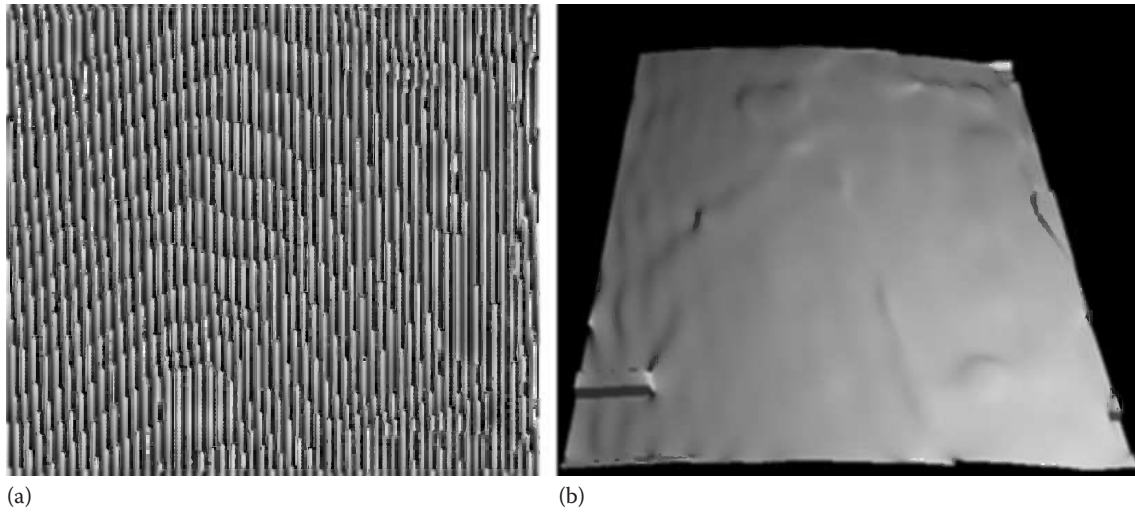


**FIGURE 7.10**  
 Wrapped phase map (a) and unwrapped phase map (b) after bringing down.

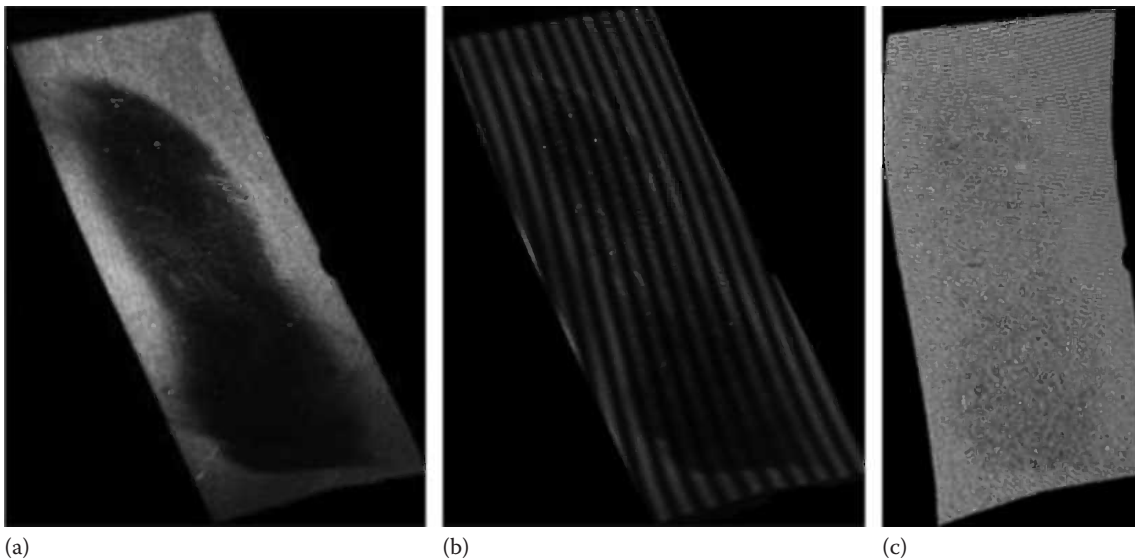


**FIGURE 7.11**  
 Shiny part measurement: (a) 2D picture, (b) fringe image, and (c) 3D point cloud.

information on a very shiny benched blade.<sup>21</sup> This surface tolerance feature makes the phase-shifting technique an excellent candidate for on-floor or in-line inspection in manufacturing because it eliminates the need for additional surface treatment of the parts to be measured.

### 7.2.3 Phase-Shifting Systems

There are various ways to do phase-shifting phase measurements. Phase-shifting systems can be classified into three categories: physical phase shifting requiring mechanical movement,<sup>5,16,22–24</sup> digital phase shifting through a digital projector without any movement,<sup>8,9,12,21</sup> and simultaneous phase-shifting techniques.

### 7.2.3.1 Physical Phase-Shifting System

In physical phase shifting, a translation stage such as a piezoelectric transducer (PZT) or other motorized stage is used to translate a component or a subsystem relative to others. In one phase-shifting Michelson interferometer,<sup>25</sup> the translated component is a mirror in the reference beam to introduce phase shifting. Many such interferometers have very high resolution with a small FOV. The relationship between the phase shift  $\varnothing$  and the translation offset  $\delta$  is calculated as ( $\lambda$  is the wavelength of the light source)

$$\varnothing = 4\pi \frac{\delta}{\lambda} \quad (7.6)$$

In a projection moiré, the grating is usually translated laterally in the grating plane in a direction perpendicular to the grating lines.<sup>26</sup> The relationship between the phase shift  $\varnothing$  and the translation offset  $\delta$  is calculated as ( $p$  is the pitch of the physical grating)

$$\varnothing = 2\pi \frac{\delta}{p} \quad (7.7)$$

In a shadow moiré system, either the grating<sup>5</sup> or the sample<sup>27</sup> can be translated. If the grating is translated, the translation is in the grating plane and Equation 7.7 is still valid. If the sample is translated, the translation direction is perpendicular to the grating and the amount of translation depends on the components and system configuration.

In a field shifting system,<sup>28,29</sup> the image-capturing unit and the fringe projection unit are translated relative to each other. The translation amount also depends on the system configuration and components for the required phase shift.

### 7.2.3.2 Digital Phase-Shifting System

In the digital phase-shifting systems as shown in Figure 7.4, a digital projector, for example LCD, DMD, and LCOS, is used to project software-generated fringe patterns with a certain intensity profile and to project a sinusoidal fringe onto the object surface. A high-resolution camera is used to capture the fringe patterns modulated by the object surface. Using phase-shifting algorithms, a relative phase map is obtained after phase wrapping and unwrapping. The  $x$ ,  $y$ ,  $z$  coordinates of the object surface with a corresponding pixel-level resolution are calculated from the phase map by use of a conversion algorithm. For a straight-line sinusoidal fringe pattern, the equation used to generate the fringe image in the computer can be written as

$$I(u, v) = \frac{M}{2} \left[ 1 + \cos \left( 2\pi \frac{u}{p} + \theta \right) \right] \quad (7.8)$$

where

$I(u, v)$  is the gray level at point  $(u, v)$  in the projector chip (LCD, DMD, or LCOS)

$p$  is the period of the fringe pattern in pixels

$M$  is the maximum grayscale the project supports

$\theta$  is the phase shift

The fringe line is along the  $v$  direction.

For a circular fringe pattern centering at  $(u_c, v_c)$ , the equation for fringe generation can be written as

$$I(u, v) = \frac{M}{2} \left[ 1 + \cos \left( 2\pi \frac{r}{p} + \theta \right) \right] \quad (7.9)$$

where

$$r = \sqrt{(u - u_c)^2 + (v - v_c)^2} \quad (7.10)$$

in which  $r$  is the calculated radius from circular fringe center  $(u_c, v_c)$  and  $I(u, v)$ ,  $p$ ,  $M$ , and  $\theta$  are the same as in Equation 7.8.

In any digital fringe pattern, the shifted phase  $\theta$  depends on the phase-shifting algorithm to be used. These phase-shifting algorithms are discussed in detail in the next section.

### 7.2.3.3 Simultaneous Phase-Shifting Techniques

The physical phase-shifting and digital phase-shifting techniques need multiple fringe images in sequence with the assumption that the target will stay still during image capturing. However, sometimes, the target has to be measured in a vibrating environment or when the target is still moving. One such example is the measurement of facial expressions. Currently, there are two ways to address this issue: one method is to capture the images in a time period as short as possible such as using three red, green, and blue (RGB) channels. But this method has limitation. The other method is to use a simultaneous phase-shifting technique to capture multiple images or multiple sub-images at the same time.

A typical solution is to project an RGB color fringe with a phase shift of  $120^\circ$  between adjacent colors and use a color camera to capture the images.<sup>8</sup> From the color image, three monochromatic images can be extracted and used to calculate the phase map via the three-step phase-shifting algorithm. The color fringe method can also be applied to projection moiré.<sup>30</sup> In one color fringe projection research,<sup>31</sup> a projected grating that consisted of RGB-colored stripes was made, each with a separate set of lines for one color channel. The three line sets were identical in terms of the fringe pitch and the fringe width. They overlapped with an offset of one-third the line pitch, resulting in a  $120^\circ$  phase shift. A color camera captured the three fringes simultaneously. For these color fringe methods, channel balance is critical to obtain low-noise phase maps from the color fringe image because the camera and the projector might not have the same response for these three color channels. A more detailed discussion is provided in the following error analysis section.

A more advanced method is to make use of the projector hardware to make “fake” color fringes.<sup>32,33</sup> When a color fringe is sent to a DMD chip of a digital projector after removing its color wheel, the three channels of the projector will have three grayscale images with a  $120^\circ$  phase shift. Because these three images are projected in 10 ms, the black-and-white camera has to be synchronized with the projector to take all three phase-shifted images in this 10 ms time frame. The 3D shape of the object surface can then be reconstructed by phase-shifting algorithms. The 3D measurement speed can reach 100 Hz. This method does not need a color camera and thus has no color balance problem.

To avoid the color balance issue, some researchers also have used polarization splitting to generate multiple interferogram channels with, for example, a  $90^\circ$  phase shift and then used multiple cameras to capture the images.<sup>34</sup> Some other methods include wave front splitting with diffraction optics such as a holographic element<sup>35</sup> or a glass plate.<sup>36</sup> In the first case,<sup>35</sup> the test and reference beams pass through a holographic element that splits the beam into four separate beams, with each beam passing through a birefringent mask before entering the charge-coupled device (CCD) camera. The four mask segments introduce phase shifts between the test and reference beams. A polarizer is placed between the phase masks and the CCD sensor, resulting in the interference of the test and reference beams. In this setup, four phase-shifted interferograms are captured in a single shot on a single camera.

---

### 7.3 Phase-Shifting Algorithms for Phase Wrapping

Although there are different measurement principles and different ways to do phase shifting, phase-shifting systems all use multiple captured fringe images and share basic phase-shifting algorithms to extract the phase map from these fringe images.

#### 7.3.1 General Phase-Shifting Algorithm

For both interferogram and projected fringes, the captured 2D fringe image can be written in the form of Equation 7.11 or 7.12:

$$I_k(i, j) = I_0(i, j) \left[ 1 + \gamma(i, j) \cos(\phi(i, j) + \theta_k) \right], \quad k = 1, 2, 3, \dots, K \quad (7.11)$$

or

$$I_k(i, j) = I_0(i, j) + I'(i, j) \cos(\phi(i, j) + \theta_k), \quad k = 1, 2, 3, \dots, K \quad (7.12)$$

where

$k$  is the index number of the images used in the phase measurement method

$I_k$  is the intensity at pixel  $(i, j)$  in the captured image

$I_0$  is the background illumination

$\gamma$  is the fringe modulation (representing image contrast)

$I'$  is the image contrast

$\theta_k$  is the initial phase for the  $k$ th image

$K$  is the total number of the fringe images

In general, it is the phase term  $\phi(i, j)$  in the fringe pattern Equation 7.11 or 7.12 that is to be calculated in the phase-shifting algorithms. In this section, attention is paid to the common discrete phase-shifting algorithms and their features. Readers interested in the development of various phase-shifting algorithms can refer to Refs. [17,37]. Also, the phase-shifting algorithms discussed in this section focus on the phase-wrapping process. Readers should keep in mind that the wrapped phase map includes the modulo  $2\pi$  discontinuity, so phase unwrapping is needed to obtain a continuous phase map.

One very helpful feature in phase-shifting systems is the calculation of the image modulation  $\gamma$ .  $\gamma$  represents the image contrast and ranges between 0 and 1. The modulation  $\gamma$  can help generate a mask to avoid problems in phase unwrapping. In industrial applications, the shape of the parts and environmental lighting conditions vary a lot and may make some areas saturated or near saturated or too dark to analyze properly. At these areas, the signal-to-noise ratio is very low and the calculated phase information may not be correct. Therefore, these locations should be excluded in the following phase-unwrapping process. These locations can be detected by the modulation  $\gamma$  because it is much smaller in these areas. A common practice is to set a threshold for  $\gamma$ . If  $\gamma$  is smaller than the threshold in a pixel, the unwrapping process should bypass it.

### 7.3.2 Common Phase-Shifting Algorithms

#### 7.3.2.1 Three-Step Phase-Shifting Algorithm

In the three-step phase-shifting algorithm,<sup>17,38</sup> the phase shift  $\theta = -2\pi/3, 0,$  and  $2\pi/3$  is used for three fringe images, respectively. The intensities of the three phase-shifted images at pixel  $(i, j)$  are

$$I_1(i, j) = I(i, j) + I'(i, j) \cos \left[ \phi(i, j) - \frac{2\pi}{3} \right] \quad (7.13)$$

$$I_2(i, j) = I(i, j) + I'(i, j) \cos [\phi(i, j)] \quad (7.14)$$

$$I_3(i, j) = I(i, j) + I'(i, j) \cos \left[ \phi(i, j) + \frac{2\pi}{3} \right] \quad (7.15)$$

In these equations, there are three unknowns:  $I, I',$  and  $\phi$ . By solving the earlier equations, phase  $\phi(i, j)$  can be obtained as

$$\phi(i, j) = \tan^{-1} \left( \sqrt{3} \frac{I_1 - I_3}{2I_2 - I_1 - I_3} \right) \quad (7.16)$$

The modulation can be calculated as

$$\gamma(i, j) = \frac{\left[ (I_3 - I_2)^2 + (2I_1 - I_2 - I_3)^2 \right]^{1/2}}{I_2 + I_3} \quad (7.17)$$

The three-step phase-shifting algorithm only needs three fringe images and thus is among the fastest discrete phase-shifting algorithms. But this algorithm is vulnerable to errors in the system such as phase-shifting error, nonlinearity error, and noise.

#### 7.3.2.2 Double Three-Step Phase-Shifting Algorithm

An improvement to the three-step phase-shifting algorithm is the double three-step phase-shifting algorithm, which can significantly reduce the error from system nonlinearity.

It has been proved that a second-order nonlinearity residual in the system can result in an error of  $\Delta\phi$  in the phase map:<sup>39</sup>

$$\tan(\Delta\phi) = \tan(\phi' - \phi) = \frac{\tan(\phi') - \tan(\phi)}{1 + \tan(\phi')\tan(\phi)} = -\frac{\sin(3\phi)}{\cos(3\phi) + m} \quad (7.18)$$

$$\Delta\phi = \arctan\left[-\frac{\sin(3\phi)}{\cos(3\phi) + m}\right] \quad (7.19)$$

where

- $\phi$  is the phase calculated with a traditional three-step algorithm when the system has perfect linearity
- $\phi'$  is the calculated phase with a traditional three-step algorithm when the system has a second-order nonlinearity
- $m$  is a constant that depends on the system linearity

Equation 7.19 indicates that the frequency of the error pattern is three times that of the fringe pattern. If an initial phase offset is introduced in the phase-shifted fringe patterns, the phase of the error wave will vary correspondingly. When two phase maps are obtained with a relative initial phase difference of  $60^\circ$ , the phase difference between these two error patterns is approximately  $180^\circ$ . Therefore, when the two phase maps are averaged, the error will be significantly reduced. This means that we can do phase shifting twice with six fringe patterns with initial phases of  $0^\circ, 120^\circ, 240^\circ$  (group one) and  $60^\circ, 180^\circ, 300^\circ$  (group two), use the three-step algorithm twice to calculate the two phase maps from each fringe group, and then average the phase maps.

The effectiveness of the double three-step algorithm can be verified theoretically. In Equation 7.19, because the second-order nonlinearity residual  $\varepsilon$  is small,  $m$  will be large. If  $m \gg 1$ , Equation 7.19 can be simplified as

$$\Delta\phi = \arctan\left[-\frac{\sin(3\phi)}{m}\right] = -\arctan\left[\frac{\sin(3\phi)}{m}\right] \quad (7.20)$$

If we introduce another phase map with an initial phase offset of  $60^\circ$  for the fringe patterns, the phase error becomes

$$\Delta\phi' = \arctan\left[-\frac{\sin(3\phi + 180^\circ)}{k}\right] = \arctan\left[\frac{\sin(3\phi)}{k}\right] \quad (7.21)$$

It is obvious that  $\Delta\phi = -\Delta\phi'$ . Therefore, if we average the two phase maps, the error will disappear.

### 7.3.2.3 Four-Step Phase-Shifting Algorithm

The four-step phase-shifting algorithm uses four fringe images with shifted phase  $\theta$  as

$$\theta_i = 0, \frac{\pi}{2}, \pi, \frac{3\pi}{2}, \quad i = 1, 2, 3, 4 \quad (7.22)$$

The four images can be written as

$$I_1(i, j) = I(i, j) + I'(i, j) \cos[\phi(i, j)] \quad (7.23)$$

$$I_2(i, j) = I(i, j) + I'(i, j) \cos\left[\phi(i, j) + \frac{\pi}{2}\right] \quad (7.24)$$

$$I_3(i, j) = I(i, j) + I'(i, j) \cos[\phi(i, j) + \pi] \quad (7.25)$$

$$I_4(i, j) = I(i, j) + I'(i, j) \cos\left[\phi(i, j) + \frac{3\pi}{2}\right] \quad (7.26)$$

Using these trigonometric functions, the phase information can be calculated as

$$\phi(i, j) = \tan^{-1}\left(\frac{I_4 - I_2}{I_1 - I_3}\right) \quad (7.27)$$

The modulation can be calculated as

$$\gamma(i, j) = \frac{2[(I_4 - I_2)^2 + (I_1 - I_3)^2]^{1/2}}{I_1 + I_2 + I_3 + I_4} \quad (7.28)$$

The four-step phase-shifting algorithm has a 90° phase shift between adjunct frames and is easier to implement in some situations, making it the most useful algorithm in simultaneous phase-shifting systems.

#### 7.3.2.4 Carré Phase-Shifting Algorithm

The Carré phase-shifting algorithm is a four-step phase shifting algorithm for use with an unknown phase shift. The four images can be written as

$$I_1(i, j) = I(i, j) + I'(i, j) \cos[\phi(i, j) - 3\theta] \quad (7.29)$$

$$I_2(i, j) = I(i, j) + I'(i, j) \cos[\phi(i, j) - \theta] \quad (7.30)$$

$$I_3(i, j) = I(i, j) + I'(i, j) \cos[\phi(i, j) + \theta] \quad (7.31)$$

$$I_4(i, j) = I(i, j) + I'(i, j) \cos[\phi(i, j) + 3\theta] \quad (7.32)$$

In this four-equation group, there are four unknowns. The phase  $\phi$  can be calculated as

$$\phi(i, j) = \tan^{-1}\left(\frac{\sqrt{3(I_2 - I_3)^2 - (I_1 - I_4)^2} + 2(I_2 - I_3)(I_1 - I_4)}{(I_2 + I_3) - (I_1 + I_4)}\right) \quad (7.33)$$

The obvious features of the Carré phase-shifting algorithm are that its constant phase step  $2\theta$  can be arbitrary and the measured phase is insensitive to all even harmonics.<sup>17,40,41</sup> Especially when the phase-shift system did not have linear response over the entire  $2\pi$  range, the Carré phase-shifting algorithm still provides good results if phase shifting is performed within a small phase-shift range in a relatively linear segment.

The Carré phase-shifting algorithm has also proved to be adaptive to variation situations because of the flexibility in phase shift.<sup>41</sup> When there is a second-order phase-shift error, the average phase measurement error can be minimized when the phase step is  $65.8^\circ$ . When there is a systematic intensity error such as a nonlinearity in camera response, the best phase step is  $103^\circ$  for the minimum phase measurement error. For a high-noise image with a random intensity measurement error, a phase step of  $110.6^\circ$  will minimize the averaged phase measurement error.

Although the four-step phase-shifting method can be considered a special case of the Carré phase-shifting algorithm, it has features that the Carré phase-shifting algorithm does not have such as an easier and faster calculation of both the phase map and modulation.

### 7.3.2.5 Five-Step Phase-Shifting Algorithm (Hariharan Algorithm)

The five-step phase-shifting algorithm with an unknown but constant phase shift is also called the Hariharan algorithm.<sup>17,42</sup> The five fringe images are

$$I_1(i, j) = I(i, j) + I'(i, j) \cos[\phi(i, j) - 2\theta] \quad (7.34)$$

$$I_2(i, j) = I(i, j) + I'(i, j) \cos[\phi(i, j) - \theta] \quad (7.35)$$

$$I_3(i, j) = I(i, j) + I'(i, j) \cos[\phi(i, j)] \quad (7.36)$$

$$I_4(i, j) = I(i, j) + I'(i, j) \cos[\phi(i, j) + \theta] \quad (7.37)$$

$$I_5(i, j) = I(i, j) + I'(i, j) \cos[\phi(i, j) + 2\theta] \quad (7.38)$$

When the phase shift  $\theta = 90^\circ$ , the phase  $\phi$  and modulation  $\gamma$  can be calculated as

$$\phi(i, j) = \tan^{-1} \left( \frac{2(I_2 - I_4)}{2I_3 - (I_1 + I_5)} \right) \quad (7.39)$$

$$\gamma(i, j) = \frac{3\sqrt{4(I_4 - I_2)^2 + (I_1 + I_5 - 2I_3)^2}}{2(I_1 + I_2 + 2I_3 + I_4 + I_5)} \quad (7.40)$$

This phase-shifting algorithm has good tolerance for phase-shift error because the first-order error terms cancel, even though the errors from second-order residuals still exist.

For an arbitrary phase shift, the phase  $\phi$  and modulation  $\gamma$  can be calculated as<sup>43</sup>

$$\phi(i, j) = \tan^{-1} \left( \frac{\sqrt{4(I_2 - I_4)^2 - (I_1 - I_5)^2}}{2I_3 - (I_1 + I_5)} \right) \quad (7.41)$$

$$\gamma(i, j) = \frac{(I_2 - I_4)^2 \sqrt{4(I_2 - I_4)^2 - (I_1 - I_5)^2 + (I_1 + I_5 - 2I_3)^2}}{4(I_2 - I_4)^2 - (I_1 - I_5)^2} \quad (7.42)$$

As with the Carré phase-shifting algorithm, the five-step phase-shifting algorithm is insensitive to phase-shift errors.<sup>44</sup>

### 7.3.2.6 Phase-Shifting Algorithms with More Than Five Steps

Although phase-shifting algorithms using more than five image frames are seldom used, they do exist.<sup>17,45,46</sup> They require more computing resources and time to process the images, and it is sometimes impossible to calculate the modulation, but they are usually more resistant to some errors. For example, a seven-sample algorithm based on the Surrel six-sample algorithm using the averaging technique was demonstrated to be insensitive to linear and quadratic nonlinear phase-shift errors with linear compensation even when the fringe signal contains a second-harmonic distortion.<sup>45</sup> Higher-order phase-shifting algorithms (six-sample, eight-sample, and nine-sample algorithms) have also been investigated to show the effectiveness in compensating for a quadratic and spatially nonuniform phase-shift error.<sup>46,47</sup>

### 7.3.2.7 Spatial Carrier Phase-Shifting Algorithms

The spatial carrier method makes use of only one high-resolution fringe image from which multiple sub-images with lower resolution are extracted, so that a multiple-step phase-shifting algorithm can be used.<sup>19,43,48–50</sup> Because the spatial carrier method uses only one fringe image, it can be used in dynamic environments such as vibrating or moving object measurements while still having the benefits of the phase-shifting techniques. Because the sub-images are obtained by selecting every  $N$ th pixel in the original image ( $N$  is the number of steps used in the phase-shifting algorithms), these sub-images have a  $1/N$  lateral resolution of the original image.

For surfaces with curvature such as edge breaks or sphere/cylindrical surfaces, the fringe pitch and thus the actual phase shifts between adjunct pixels can vary a lot over the entire surface. When the spatial carrier technique is used, it is critical to select phase-shifting algorithms with an unknown phase shift such as the Carré phase-shifting algorithm or the five-step phase-shifting algorithm with an arbitrary phase shift, as discussed in previous sections. For these algorithms, the local curvature has a decisive impact on the measurement accuracy.

The spatial carrier method is sensitive to random noise and is less tolerant to surface finish variation. Unlike traditional phase-shifting algorithms, where at corresponding pixel  $(i, j)$  the detected intensities  $I_k$  of these  $K$  fringe images come from the same physical location on the surface, in the spatial carrier technique, the intensity  $I_k(i, j)$  corresponds to different physical locations (adjunct pixels in the original image). Therefore, any variation in the surface reflection or scattering angle, the surface finish, the illumination angle, and random noise may result in an error in the wrapped phase using traditional phase-shifting algorithms.

### 7.3.3 Selection of Phase-Shifting Algorithms

Many different phase-shifting algorithms have been developed in the past that can be used to reduce different types of errors. Because each algorithm has its own features and

no single algorithm can meet all requirements, selection of the most appropriate phase-shifting algorithm for a specific phase-shifting measurement system needs careful analysis and trade-off considerations.

System dependence results from the fact that different systems have their own main error sources. For digital phase-shifting systems, phase shift is performed by software programming, and there is no phase-shifting error. The main error sources become the nonlinearity and noise from the camera and projector. Those phase-shifting algorithms that are insensitive to the system nonlinearity will provide the best measurement results. On the contrary, for physical phase shifting, the phase-shifting error is usually one of dominant error sources. When using a physical phase-shifting method, the algorithms that are insensitive to the phase-shift error will work best. In general, for incorrectly calibrated linear error and some nonlinear errors, algorithms that can work with an unknown phase shift such as the Carré phase-shifting algorithm and the five-step phase-shifting algorithm work the best. For simultaneous phase-shifting systems, the misalignment of multiple cameras or sub-images on the same camera may be the critical problem, and the selected algorithm needs to work in this situation.

Other considerations are more application oriented. Factors to consider include the part geometric (especially curvature variation and surface finish), measurement speed requirement, measurement environment, and accuracy requirements.

---

## 7.4 Phase-Shifting System Modeling and Calibration

Phase-shifting algorithms for phase wrapping result in a phase map with a  $2\pi$  ambiguity. To remove the  $2\pi$  ambiguity, a phase-unwrapping process is needed. A continuous phase map  $\Phi(i, j)$  can be obtained after phase unwrapping. This phase map contains geometric information about the measured surface that sometimes looks like an unscaled, distorted 3D surface contour of the object. However, the phase value of the unwrapped phase map depends on the starting point of the unwrapping process. Thus, from a unique wrapped phase map  $\phi(i, j)$ , there may be many unwrapped phase maps  $\Phi(i, j)$  that can be obtained. Furthermore, a digitized geometry is usually represented by a point cloud with a set of 3D coordinates for each point, not the phase map. Converting from the continuous phase map to coordinates of the surface points is a critical process for accurate measurement, which requires a unique absolute phase map, system modeling, and system calibration.

### 7.4.1 Modeling of Phase-Shifting Measurement System

The phase map from the phase-shifting process contains information about an object profile and may be similar to its 3D shape, but the phase map and the profile are not the same. For industrial applications, it is the surface profile not the phase map that is desired. Once the phase map is obtained from the image(s), the coordinates at the sampled points on an object surface must be further calculated. This coordinate calculation at the sample points has to do with a conversion algorithm from phase map to coordinates through modeling.<sup>19</sup> Based on system configuration requirement and object complexity, current models for phase-coordinated conversion can be classified into three categories: linear model, partially linear model, and nonlinear model.

#### 7.4.1.1 Unwrapped Phase Map and Absolute Phase Map

Before further discussing the model for phase-coordinated conversion, some clarification is needed for the term “absolute phase map.” Absolute phase map was initially used by some researchers to stand for a continuous phase map without  $2\pi$  discontinuity<sup>51</sup> such as the unwrapped phase map. Nowadays, it represents the phase map that is used to be converted to coordinates.

For a linear or partially linear model, the absolute phase map is usually obtained by subtracting a reference phase map from the measurement phase map. The measurement phase map is the unwrapped phase map after performing phase shifting on the object surface. Reference phase maps can be obtained by either performing phase shifting on a reference plane (usually flat) or by creating a flat phase plane determined by specific points (constituting a horizontal and a vertical line) on the measurement phase map. The coordinates calculated later will be referred to these planes. After subtraction, the measurement phase map is brought down. In the unwrapping process for both the measurement phase map and the reference phase map, the starting point for the unwrapping processing should be the same.

For a nonlinear model, an absolute phase map is linked to the coordinates system through either a projector or a camera. For physical phase shifting, special components with unique features can be used such as the seam of a folded mirror and overlapped points or seam or similar features. For digital phase shifting, an additional single-line segment or some kind of special pattern can be projected. These lines or patterns have known physical position in the projector and make it much easier to build the relationship between the phase value and physical location to further obtain the absolute phase map directly related to the system geometry.

One such example is the absolute phase map for the master gage shown in Figure 7.7. The digital phase-shifting system used to measure the master gage is similar to the configuration shown in Figure 7.4, which consisted of a black-and-white CCD camera, a digital light processing (DLP) projector with DMD technology, an image processor board (Matrox Genesis), a PC workstation, and windows-based software for system control and data processing. To obtain the absolute phase map, a vertical centerline through the center of the projector DLP chip was projected to the object surface. The captured centerline image is shown in Figure 7.12. The purpose is to correlate every pixel in the phase map to a point on the DMD chip of the projector.

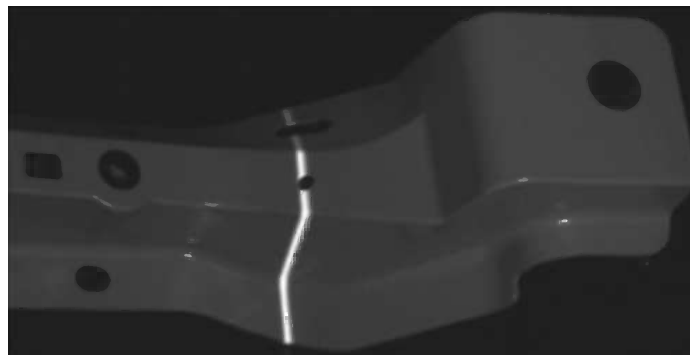


**FIGURE 7.12**  
Image of the projected centerline.

The centerline image was used to identify the pixels in the phase map that correspond to the centerline in the projector chip. These pixels should have the same absolute phase as that of the centerline of the projection field where the project fringe patterns were programmed. With the absolute phase at these pixels known, the absolute phase map of the entire surface can be obtained by simply translating the relative unwrapped phase map  $\Phi(i, j)$ . Assume the absolute phase of the centerline to be  $\Phi_0$ . The absolute phase map  $\Phi'(i, j)$  can be obtained as follows:<sup>38</sup>

$$\Phi'(i, j) = \Phi(i, j) + \Phi_0 - \frac{1}{N} \sum_{k=1}^N \Phi_k \quad (7.43)$$

where

$\Phi_k$ 's are the phases of the pixels that correspond to the centerline of the projection field  
 $N$  is the total number of such pixels in a specified segment

The number  $N$  may be smaller than the total number of vertical pixels of the CCD sensor because the centerline may hit openings on the object surface and line centers near the openings should be excluded from calculation. Theoretically, the absolute phase at just one pixel is enough to obtain the entire absolute phase map of the object. However, by taking the average of the absolute phase values at multiple pixels, as is done in Equation 7.43, more accurate results can be obtained.

In digital phase shifting, some techniques other than the additional line projection have also been investigated such as embedded patterns or features in the fringe patterns.<sup>52,53</sup> Interested readers can find details in these papers.

#### 7.4.1.2 Linear Model for Flat Surface Measurement

As a simple model that many researchers like to use, the linear model is very straightforward: the lateral dimensions are proportional to the pixel index while the vertical dimension is proportional to the absolute phase after reference phase subtraction. The calculation that converts pixel  $(i, j)$  with absolute phase  $\Phi'$  to coordinates  $(x, y, z)$  can be represented by the following formulae:<sup>53,54</sup>

$$x = K_x(i - C_x) \quad (7.44)$$

$$y = K_y(j - C_y) \quad (7.45)$$

$$z = k_z \Phi' \quad (7.46)$$

where

$K_x, K_y, K_z$  are scalars in the three coordinate directions  
 $(C_x, C_y)$  are specified coordinate origin in the lateral directions

In practice,  $K_x$  and  $K_y$  are usually determined by calibration in the FOV and  $K_z$  is determined by step gage standards.

It is obvious that the linear model requires the camera viewing direction to be perpendicular to the object surface. This model is usually used in flat surface measurement only.

A good example is the shadow moiré technique used for flatness measurement in printed circuit boards (PCB), where the shadow moiré technique has been specified in several industrial standards as a warpage measurement tool.<sup>55,56</sup>

#### 7.4.1.3 Partially Linear Model for Flat Surface Measurement

The partially linear model assumes that some dimensions (usually  $x$  and  $y$  coordinates) are proportional to the pixel index ( $i, j$ ) on the image while the vertical coordinate is calculated from the absolute phase value using a nonlinear formula.

To deduce this kind of functions, some assumptions must be made such as assuming the camera is at the same height as the grating and/or assuming the optical axis of the camera/lens is perpendicular to the object surface. Using this method, the system configuration of a fringe projection system can be simplified as shown in Figure 7.13. Let  $(C_x, C_y)$  be the intersect of the camera sensing surface and the optical axis of the imaging lens; the coordinates  $(x, y, z)$  can be calculated as

$$x = K_x(i - C_x) \quad (7.47)$$

$$y = K_y(j - C_y) \quad (7.48)$$

$$z = h = \frac{L \times \Phi'}{\Phi' - 2\pi f D} \quad (7.49)$$

where  $K_x, K_y$  are scalars in the lateral directions determined by calibrating the FOV. In Equation 7.49,  $\Phi'$  is the absolute phase, that is, phase difference at pixel  $(i, j)$  between the flat reference plane and the object plane, and  $f$  is the average frequency of fringe on reference plane.  $\Phi'$  can be obtained by either subtracting the object phase map from the phase map of the reference plane or by removing the slope in the measurement phase map by bringing down the phase map. Equation 7.49 is not a universal function. Depending on system configurations, other similar functions may be derived.<sup>57</sup>

Under some situations, Equations 7.47 through 7.49 can provide reasonably good results, especially for measurements on flat surfaces. But there are so many assumptions in this particular analysis that they cannot provide the desirable accuracy for curved surface measurement. For example, in Figure 7.13, there is no way to ensure that the camera and fringe

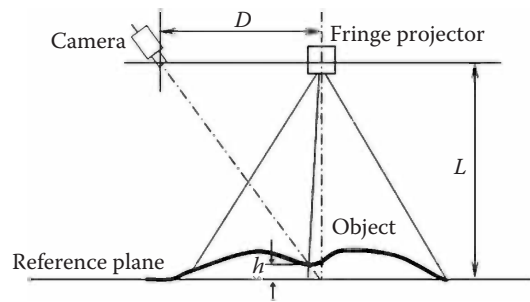


**FIGURE 7.13**  
Simplified system configuration to calculate coordinate  $z$ .

projection unit are exactly at the same height. Furthermore, for complicated surface shapes with various curvatures, or in a configuration where there is no good means to ensure the object is perpendicular to the axis of the imaging system, due to magnification variation from point to point, the  $x$  and  $y$  coordinates are no longer proportional to the image index  $(i, j)$ . The errors in the measured shape of complex surfaces can be very obvious when the measured result is compared with a model or other data measured from a good coordinate measurement machine (CMM).

When  $L \gg h$ , Equation 7.49 can be further simplified as

$$z = k_z \Phi' \quad (7.50)$$

where

$$k_z = -\frac{L}{2\pi fD} \quad (7.51)$$

In this case, the partially linear model is simplified to the linear model represented in Equations 7.44 through 7.46.

#### 7.4.1.4 Nonlinear Model for Complex Shape

To obtain more accurate results, a more thorough nonlinear model than the linear and partially linear models is needed. To demonstrate the concept of the nonlinear model, the key dimensions of the digital fringe projection system of Figure 7.4 are shown in Figure 7.14. In this diagram,  $L$  is the imaging lens center,  $R$  is the projection lens center, and the global coordinate system  $XYZ$  has its origin at point  $O$ .

The 3D coordinates  $(x, y, z)$  of any corresponding object point  $P$  with an image pixel  $Q(i, j)$  and absolute phase value  $\Phi'(i, j)$  can be calculated uniquely in the 3D space. First, all points on each vertical light sheet  $RP$  of the fringe pattern have the same phase, so the positions of the fringe lines on the projector can be calculated from the absolute phase values  $\Phi'$ . The equation of the light sheet  $RP$  with phase  $\Phi'(i, j)$  can be stated as

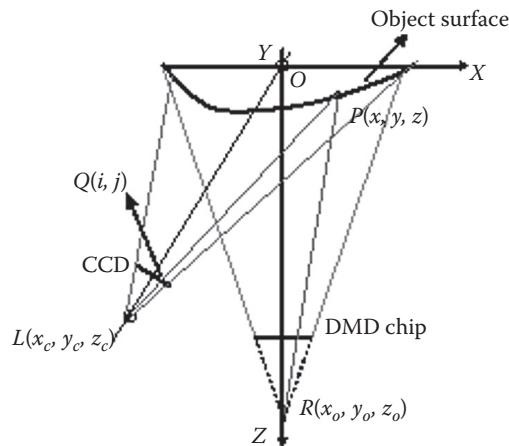


FIGURE 7.14

Diagram for a digital phase-shifting system with a DLP projector.

$$A(\Phi', i, j, c...)x + B(\Phi'', i, j, c...)y + C(\Phi', i, j, c...)z = D(\Phi', i, j, c...) \quad (7.52)$$

where  $A$ ,  $B$ ,  $C$ , and  $D$  define the function of the light sheet  $RP$  with phase value  $\Phi'(i, j)$ , image index  $(i, j)$ , and system parameters  $c$ . On the other hand, in the imaging system, the object point  $P$  should lie at the line that connects image pixel  $Q(i, j)$  and the camera lens center  $L(x_c, y_c, z_c)$ . The equation of this line  $LQ$  can be written as

$$\frac{x - x_c}{l} = \frac{y - y_c}{m} = \frac{z - z_c}{n} \quad (7.53)$$

where  $(l, m, n)$  is the direction vector of the line.

Calculating the intersection between the imaging ray  $LQ$  and projection light sheet plane  $RP$  by solving Equations 7.52 and 7.53 will provide coordinates  $(x, y, z)$  for any point  $P$  on the object surface.

This model works for all system configurations and complex surfaces. Unlike linear and partially linear models, it provides not only accurate shape but also space location of this surface in a global coordinate system determined in a calibration process, thus enabling data merging from multiple measurements<sup>58</sup> and accurate 360° shape reconstruction.<sup>59</sup> Figure 7.15 shows a reconstructed 360° shape of a flowerpot with complex surface textures from three measurements. Note that the steps between adjacent patches near the top edge result from magnification changes in the FOV between these measurements due to the tilting of the camera.

#### 7.4.2 Phase-Shifting System Calibration

No matter which phase-to-coordinate conversion model is used, a calibration process has to be performed to determine the system parameters that are required by the conversion algorithms for the calculation of the object coordinates. This calibration process can be as simple as estimating the FOV and measuring a step gage with known step height as for a linear model and some partially linear models. However, in order to obtain accurate measurement results, a more complex calibration process is either desirable for lens error compensation or is desired for the nonlinear model.

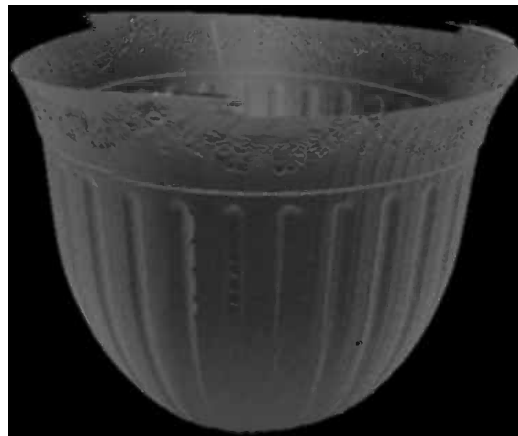


**FIGURE 7.15**  
Reconstructed 360° shape of a flowerpot with complex surface textures.

A calibration process is in fact an optimization process that finds a set of parameters to minimize the errors in the data collected for calibration. The ultimate goal of a calibration process is to find the systematic parameters that are used in the previous model for coordinate calculation of the object surface. These parameters are sometimes referred to as extrinsic parameters. Some calibration methods also have the capability to find intrinsic parameters to compensate for the imperfection in alignment, imaging lens, and cameras. Various calibration processes have been investigated,<sup>38,60–66</sup> among which Tsai calibration<sup>60</sup> using a well-aligned calibration target on a translation stage and Zhang calibration<sup>61</sup> using a check board placed in the 3D space with different orientations are most widely used and have many adaptive forms.

#### 7.4.2.1 Camera Calibration

A camera model describes the mapping between points in a 3D space and a pixel in the 2D camera sensor chip. The parameters in a camera model can be classified into intrinsic parameters, which describe the geometry of the camera itself, and extrinsic parameters, which determine the camera's pose in the 3D space. Camera calibration is a process to find these intrinsic and extrinsic parameters. Thanks to high-quality imaging lens in the optical industry, a simplified pinhole camera model<sup>67</sup> can often meet the accurate calibration requirement, although more complex camera models have also been investigated.<sup>68,69</sup> The pinhole model is demonstrated in Figure 7.16. Assuming the focus length of the imaging lens is  $f$ , a point  $P(x, y, z)$  in the 3D space can be projected into the 2D image plane at image point  $Q(u, v)$  as

$$u = \frac{fx}{z} \quad (7.54)$$

$$v = \frac{fy}{z} \quad (7.55)$$

In this section, we briefly introduce Tsai and Zhang calibration methods, both of which are based on the pinhole camera model. Interested readers are referred to the referenced papers for more details about various camera models and related calibration techniques. Although there are many calibration toolkits available on the Internet, it is highly recommended that

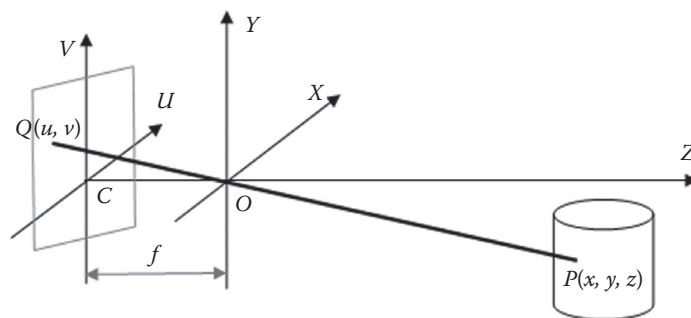


**FIGURE 7.16**  
Pinhole camera model.

the related camera models for these toolkits be fully understood because different models may use the same terms for different meanings.

The Tsai camera calibration method can deal with coplanar and noncoplanar points. It is a two-step calibration method that can calibrate the intrinsic and extrinsic parameters separately. In Tsai calibration, there are 11 parameters that are to be optimized:

$f$ : Effective focal length of the camera lens

$k$ : Radial distortion coefficient of the camera lens

$(C_x, C_y)$ : Origin of the image coordinate (intersect of the lens axis and the image sensor)

$S_x$ : Scale factor due to imperfections in hardware timing misstep

$(R_x, R_y, R_z)$ : Rotation angles between the global and camera coordinates systems

$(T_x, T_y, T_z)$ : Translation position between the global and camera coordinates systems

The rotation matrix  $R$  is deduced from the  $(R_x, R_y, R_z)$  as

$$R = \begin{bmatrix} r_1 & r_2 & r_3 \\ r_4 & r_5 & r_6 \\ r_7 & r_8 & r_9 \end{bmatrix} \quad (7.56)$$

where

$$r_1 = \cos(R_y)\cos(R_z) \quad (7.57)$$

$$r_2 = \sin(R_x)\sin(R_y)\cos(R_z) - \cos(R_x)\sin(R_z) \quad (7.58)$$

$$r_3 = \sin(R_x)\sin(R_z) + \cos(R_x)\sin(R_y)\cos(R_z) \quad (7.59)$$

$$r_4 = \cos(R_y)\sin(R_z) \quad (7.60)$$

$$r_5 = \sin(R_x)\sin(R_y)\sin(R_z) + \cos(R_x)\cos(R_z) \quad (7.61)$$

$$r_6 = \cos(R_x)\sin(R_y)\sin(R_z) - \sin(R_x)\cos(R_z) \quad (7.62)$$

$$r_7 = -\sin(R_y) \quad (7.63)$$

$$r_8 = \sin(R_x)\cos(R_y) \quad (7.64)$$

$$r_9 = \cos(R_x)\cos(R_y) \quad (7.65)$$

The translation matrix  $T$  is defined as

$$T = \begin{bmatrix} T_x \\ T_y \\ T_z \end{bmatrix} \quad (7.66)$$

A point  $(x, y, z)$  in the world coordinate system is transformed to the image coordinate system to be  $(x_i, y_i, z_i)$  through the translation matrix  $T$  and rotation matrix  $R$  as

$$\begin{bmatrix} x_i \\ y_i \\ z_i \end{bmatrix} = R \begin{bmatrix} x \\ y \\ z \end{bmatrix} + T \quad (7.67)$$

Further transformation to undistorted coordinates  $(x_u, y_u)$  to distorted  $(x_d, y_d)$  in image plane coordinates via the pinhole model is

$$x_u = \frac{fx_i}{z_i} \quad (7.68)$$

$$y_u = \frac{fy_i}{z_i} \quad (7.69)$$

$$x_d = \frac{x_u}{1 + kr^2} \quad (7.70)$$

$$y_d = \frac{y_u}{1 + kr^2} \quad (7.71)$$

where  $k$  is the lens distortion coefficient and  $r = \sqrt{x_d^2 + y_d^2}$ .

The transformation from distorted coordinates  $(x_d, y_d)$  to the final image index  $(x_f, y_f)$  is

$$x_f = \frac{s_x x_d}{d_x} + C_x \quad (7.72)$$

$$y_f = \frac{y_d}{d_y} + C_y \quad (7.73)$$

where  $(d_x, d_y)$  are camera pixel size in the  $X$  and  $Y$  direction.

In Tsai's calibration, a calibration setup is required for calibration data preparation. In this setup, a flat target with certain patterns is mounted to a translation stage with the target plane perpendicular to the translation direction. The target is translated in the calibration volume (usually as close to the measurement volume as possible). At each location, the image of the target is taken and saved with the translation reading. The  $X$  and  $Y$  axes origin is specified on the target (usually in the middle), while the translation direction defines the  $Z$  axis with one translation location set as  $Z=0$ . After processing the target images, for each feature on the calibration target, a unique correspondence between the real image index  $(x_f, y_f)$  in the image plane and its 3D coordinates  $(x, y, z)$  in the calibration volume is established. Applying this data set to the Tsai's calibration algorithm, together with known information about the camera and lens, all optimized intrinsic and extrinsic parameters can be obtained.

The Zhang camera calibration describes the relation between point  $(x, y, z)$  in the 3D space and image point  $(u, v)$  in the image plane in another form as

$$s \begin{bmatrix} u \\ v \\ 1 \end{bmatrix} = \begin{bmatrix} \alpha & \gamma & u_0 \\ 0 & \beta & v_0 \\ 0 & 0 & 1 \end{bmatrix} \underbrace{\begin{bmatrix} \mathbf{r}_1 & \mathbf{r}_2 & \mathbf{r}_3 & \mathbf{t} \end{bmatrix}}_{[\mathbf{R} \ \mathbf{t}]} \begin{bmatrix} x \\ y \\ z \\ 1 \end{bmatrix} \quad (7.74)$$

where

$s$  is an arbitrary scale factor

$[\mathbf{R} \ \mathbf{t}]$  is the transformation matrix containing the extrinsic parameter

scale matrix  $A$  contains the intrinsic parameters

$$A = \begin{bmatrix} \alpha & \gamma & u_0 \\ 0 & \beta & v_0 \\ 0 & 0 & 1 \end{bmatrix} \quad (7.75)$$

Physical meanings of these parameters are

$\alpha$ : Effective focal length in the image  $u$  axis

$\beta$ : Effective focal length in the image  $v$  axis

$\gamma$ : Skewness factor of the  $u$  and  $v$  axes in the image plane

$\mathbf{R}$ : Rotation matrix consisting of three column vectors  $\mathbf{r}_1$ ,  $\mathbf{r}_2$ , and  $\mathbf{r}_3$

$\mathbf{t}$ : Translation matrix

$(u_0, v_0)$ : Coordinates of the principal point

$(k_1, k_2)$ : Two coefficients of the radial distortion

The distorted image coordinates  $(u', v')$  are related to the undistorted image coordinates  $(u, v)$  as

$$u' = u + (u - u_0) \times (k_1 r^2 + k_2 r^4) \quad (7.76)$$

$$v' = v + (v - v_0) \times (k_1 r^2 + k_2 r^4) \quad (7.77)$$

where

$$r = \sqrt{(u - u_0)^2 + (v - v_0)^2} \quad (7.78)$$

Zhang calibration first solves five intrinsic parameters and all extrinsic parameters using a closed-form solution and then estimates the coefficients of the radial distortion by use of a linear least-square algorithm (note: this estimate may be inexact as actual optical geometric distorting in a lens goes as a cube function).

In Zhang's calibration, there is no need for the translation stage. A flat target with certain patterns is placed at a minimum of three orientations: the first one at zero position for the Z coordinate, and then the others skewed relative to the first one. The motion of the target is flexible and need not be known. The X and Y origin is specified on the target. At each orientation, an image is taken and processed to obtain the calibration data set. By running the calibration codes with the data set and known parameters about the camera and lens, the parameters can be obtained.

In either Tsai calibration or Zhang calibration, an appropriate image processing is required. The calibration target needs to have features that are easy to identify and with known physical dimension. Common patterns include dot patterns, donut patterns, checkboard patterns, square grid patterns, and line grids. Either the center or edge corner on these patterns can be used as calibration features. Some researchers also use coded marks.<sup>70</sup>

In phase-shifting measurement systems, the calibrated parameters are used to calculate the 3D coordinates from each camera pixel and its phase information. Unlike calibration that starts from known 3D coordinates of target features in the 3D space, measurement has to start with the pixel index to calculate coordinates in the 3D space. This requires full understanding of the calibration model and properly using these parameters in a reverse way.

#### 7.4.2.2 Projector Calibration

In general, projector calibration can be regarded as a reverse of the camera calibration using the same pinhole model. Although a projector cannot take images like a camera, it can project a pattern with known pixel information ( $u, v$ ) on the projector chip such as a known grid or stripe. In Tsai calibration, the projector can be calibrated with the same setup as the camera calibration discussed in the previous section because the projected pattern on the calibration target can be captured by the camera. After camera calibration, the calibrated results can be used to calculate the coordinates ( $x, y, z$ ) of the projected features such as grid points in the 3D space at some known Z locations. In this way, the correspondence between projector pixel ( $u, v$ ) and related 3D coordinates ( $x, y, z$ ) in the 3D space is established. The obtained data set can then be applied to the calibration algorithm to obtain the projector calibration parameters. It should be noted that, in this way, the projector and camera are calibrated in the same global coordinates system. Figure 7.17 shows one captured image of the projected grid pattern on a calibration target while Figure 7.18 shows the point clouds of the data set obtained at 5 Z positions for projector calibration.

Also, individual points can be projected as well to collect the data, instead of the grid. C. Sinlapeecheewa used the stereo vision method to obtain the 3D coordinates of the project point with a known pixel location in the projector chip.<sup>71</sup> Another researcher used CMM to place the target at specified 3D coordinates.<sup>72</sup>

A good use for the projector calibration with the grid data set is the masking on the projector.<sup>21</sup> A mask is a binary image that describes which pixel is valid. In the digital phase-shifting systems, both projected and captured images are programmable. To take advantage of this programmability to deal with double bounce light (light that reflects from one area on a part to another, causing confusing patterns), we can use masks to control where to project fringes and where to be measured. A fringe mask can be applied to the fringe projection unit so as to only illuminate a specific area. Because phase shifting-based fringe projection is a pixel-independent (each pixel is calculated independently) method, an image mask can be used to obtain measured data only on selected small patch of the part. By use of masks, we can easily divide the part into several measurement patches and

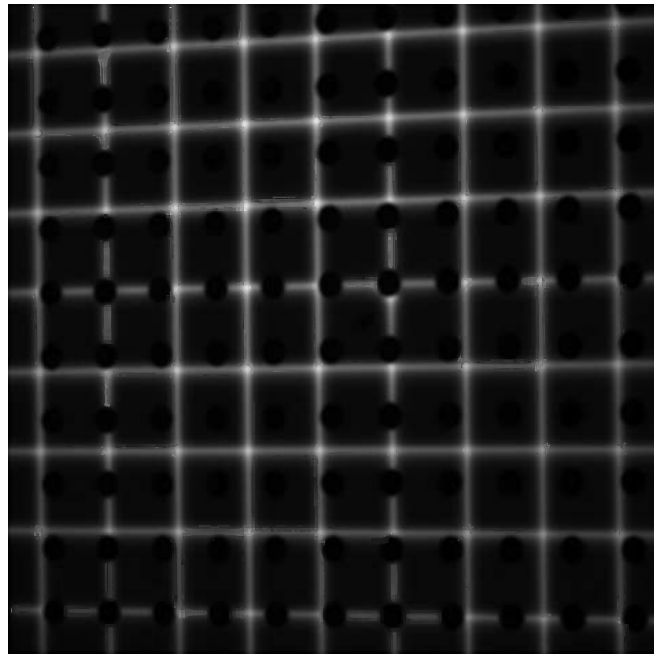


**FIGURE 7.17**  
Projected grids on the calibration target with dot patterns.

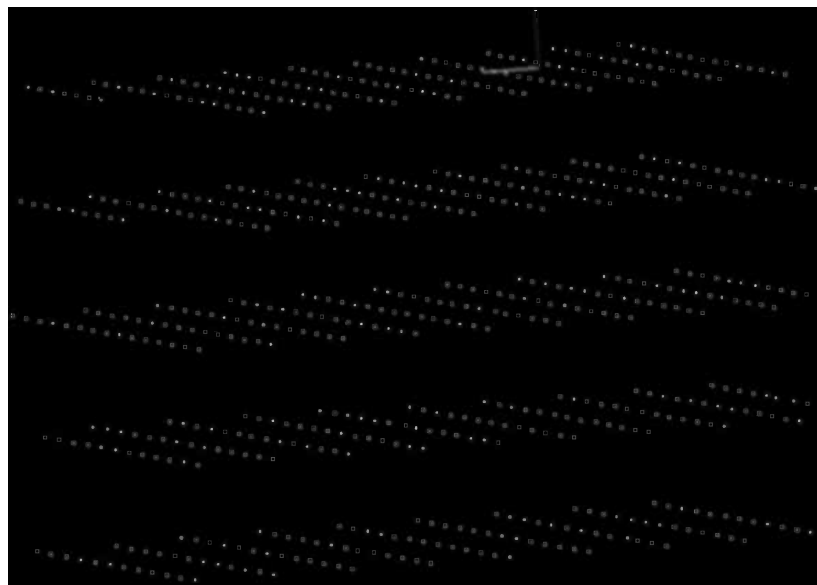


**FIGURE 7.18**  
Point cloud of the projected grid points on the target at 5 Z positions.

measure them separately. The fringe mask can be generated from a previous point cloud, manually selected mask border, or a 3D model at a known location.

Another way to calibrate the projector is to use a stripe data set instead of grid data set. When straight-line fringe patterns are used in the digital phase-shifting systems, in order to use the nonlinear model for phase-to-coordinate conversion, we need the light sheet orientation information that corresponds to an absolute phase value. It is known that a plane

in 3D space can be interpolated from two known 3D planes called base planes. Assuming the two base planes have equations  $A_1x + B_1y + C_1z + D_1 = 0$  and  $A_2x + B_2y + C_2z + D_2 = 0$ , for a phase value  $\Phi'$ , the pixel location  $\delta$  in the projector chip is ( $p$  is the pitch of the digital fringe pattern)

$$\delta = \frac{p\Phi'}{2\pi} \quad (7.79)$$

whose corresponding light sheet plane in the global coordinate system can be determined as

$$A_1x + B_1y + C_1z + D_1 + \delta \times (A_2x + B_2y + C_2z + D_2) = 0 \quad (7.80)$$

To find the base plane equations, multiple line strips with known stripe location (determined by pixel number on the projector chip) can be projected onto the calibration target whose image is captured by the camera during calibration at each position. Similar to grid image processing, at each known  $Z$  position, the images of these stripes can be processed and the 3D coordinates of these strip lines on the target can be obtained after the camera calibration is performed. Figure 7.19 shows the captured stripe image, and Figure 7.20 the processed 3D coordinates in the 3D space. With this data set, the two base plane equation parameters  $(A_1, B_1, C_1, D_1)$  and  $(A_2, B_2, C_2, D_2)$  can be obtained through fitting.

When Zhang calibration is used in the camera calibration, no  $Z$  position is available for grid or strip image processing to obtain 3D point clouds. In this case, a link between the camera and the projector has to be established for the projector calibration.<sup>63,73</sup> The basic idea is to map the CCD image to the projector chip to form a so-called projector image. First, the vertical and horizontal fringes with additional centerline stripes are projected, and phase shifting is performed to obtain the absolute phase map in both the horizontal and the vertical directions as in regular phase shifting. The horizontal absolute phase map  $\Phi'_x$  and vertical absolute phase map  $\Phi'_y$  are saved to map the camera pixel to the projector pixel. At each orientation during calibration, the same checkerboard is used for the camera calibration and projector calibration, and grayscale images capturing and phase shifting

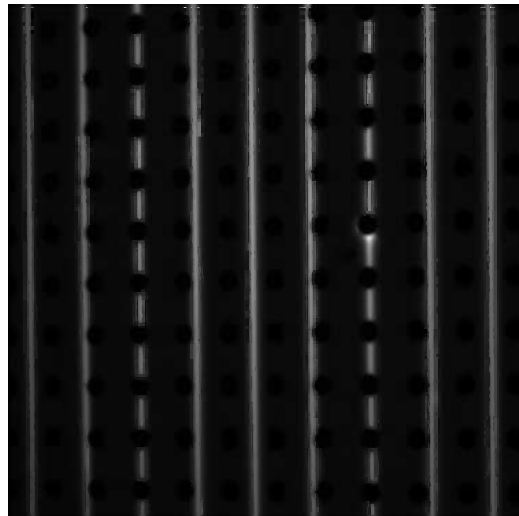


**FIGURE 7.19**  
Projected stripes on the calibration target with dot patterns.

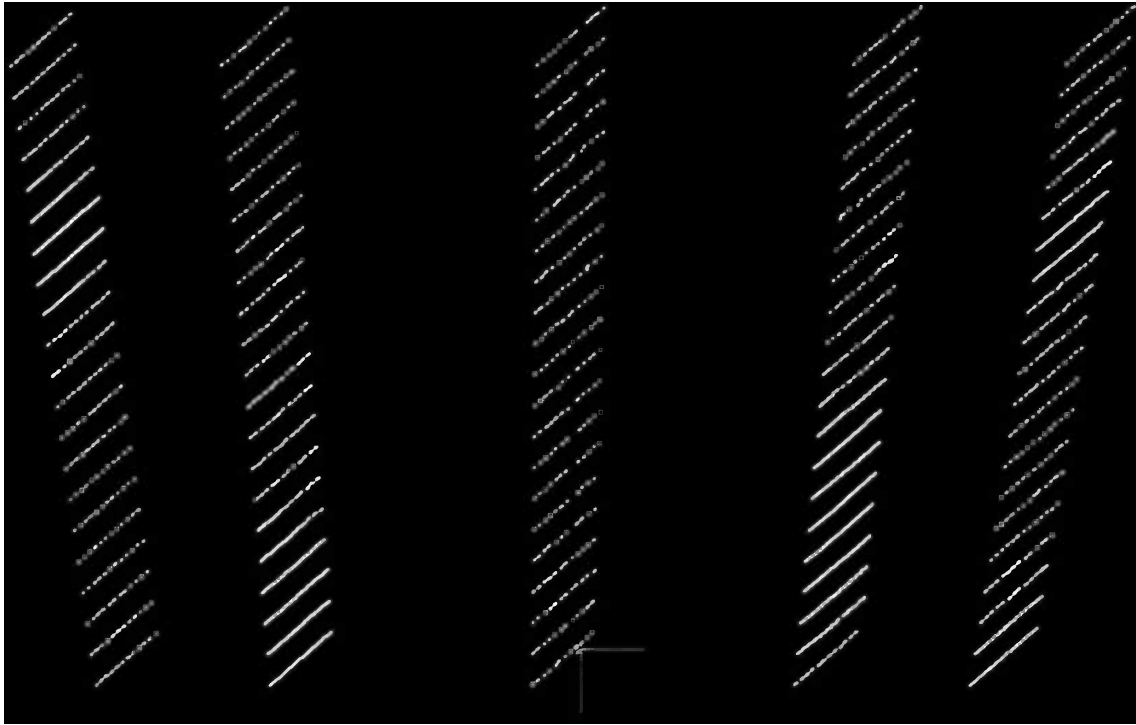


**FIGURE 7.20**

Point cloud of the projected five stripes on the target at 21 Z positions.

on the checkerboard are performed. First, the grayscale images of the checkerboard are processed for camera calibration using Zhang's calibration model. For each feature (corner of the squares) on the CCD image, its pixel index  $(i, j)$  can be mapped to the projector index  $(u, v)$  as  $(p_x$  and  $p_y$  are the pitches of the fringes)

$$u = \frac{p_x \Phi'_x(i, j)}{2\pi} \quad (7.81)$$

$$v = \frac{p_y \Phi'_y(i, j)}{2\pi} \quad (7.82)$$

The checkerboard's feature locations and their corresponding projector index  $(u, v)$  are then used for projector calibration just as in camera calibration. Because the same checkerboard is used for both phase shifting and calibration, a special colorful pattern is often used to ensure high-contrast images are available for both purposes.<sup>63</sup>

---

## 7.5 Error Analysis and Compensation for Phase-Shifting Systems

As in any other optical instrument, the phase-shifting measurement system should always use the most reliable and best-quality components if they are available and affordable. The reason is obvious: a carefully designed lens with very little distortion

is more likely to provide better results than using a low-quality lens with software-based lens distortion correction; setting the projector gamma to linear is better than compensating for a nonlinear gamma curve in a projector. Moreover, coupling among different error sources may make the error compensation less efficient and more difficult. In addition, care has to be taken in system adjustment such as alignment and focusing/defocusing. With that said, error correction and compensation are still very useful as a last means of obtaining high-quality measurement results although it makes sense only after a “best” system is built.

### 7.5.1 Error Sources and Adjustment in the Phase-Shifting System

There are many error sources in an optical phase-shifting measurement system.<sup>74,75</sup> This section discusses the major and most common error sources and their behaviors.

#### 7.5.1.1 Phase-Shifting Error

In digital phase-shifting systems, the phase shift is generated in a software program, and theoretically, there is no phase-shift error. In physical phase shifting, linear phase-shift error from stage miscalibration and nonlinear phase-shift error from poor stage response or control are one of the major concerns.<sup>22</sup>

A phase-shift error can sometimes be observed as ripples in averaged grayscale images. For example, in a three-step phase-shifting algorithm, the averaged image of the three fringe images should not have any ripple. Adding Equations 7.12 through 7.14, the averaged image  $\bar{I}$  can be calculated as

$$\bar{I} = \frac{I_1 + I_2 + I_3}{3} = I(i, j) \quad (7.83)$$

which is a uniform background image whose brightness is about half of the maximum brightness.

If one image has a phase-shift error, the averaged image will have significant ripples. Figure 7.21 shows the averaged image of three simulated fringe images with a phase shift of 0°, 120°, and 245°.

One option to reduce the phase-shift error in physical phase-shifting systems is to use a very linear phase shifter and carefully calibrate the stage response to determine voltage or pulse signal. Another option is to select a phase-shift algorithm that is insensitive

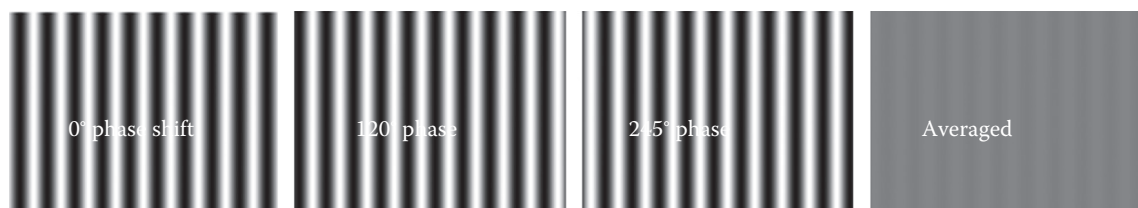


**FIGURE 7.21**

Ripples on the averaged image when the third fringe has a 5° phase-shift error.

to the phase-shift error such as the Carré phase-shifting and five-step phase-shifting algorithms.

### 7.5.1.2 Nonlinearity Error in the Detector/Projector

Nonlinearity errors may exist in both the camera and the projector. For industrial digital cameras, even though most have very good linearity unless the camera gain is set too low or too high, second-order nonlinearity may still exist. For presentation and home theater digital projectors, the default gamma setting is usually nonlinear because it is set for visual perception of nonlinear human eyes. Some projectors allow the users to reset gamma to be linear, but second-order nonlinearity may still exist. As one of the most severe error sources in digital phase-shifting systems, the nonlinearity will have to be compensated, which is discussed in more detail in the following sections.

A typical nonlinearity gamma curve is shown in Figure 7.22. This curve was obtained by inputting uniform grayscale images at 1 grayscale step up to 8 bits data limit (255 grayscale maximum) to a Canon SX50 LCOS projector. For each of the nine available gamma settings (from  $-4$  to  $4$ ), a 12 bits digital QImaging camera was used to capture images of the projected uniform pattern on a white diffusive target for each projected grayscale image. The curves show nonlinearity from both the camera and the projector, mainly from the projector.

Some phase-shifting algorithms can deal with the nonlinearity error. For example, it has been proved that the double three-step phase-shifting algorithm is very efficient in eliminating the second-order nonlinearity error in the imaging/projecting system,<sup>39</sup> even if the second-order nonlinearity comes from the camera or the projector.

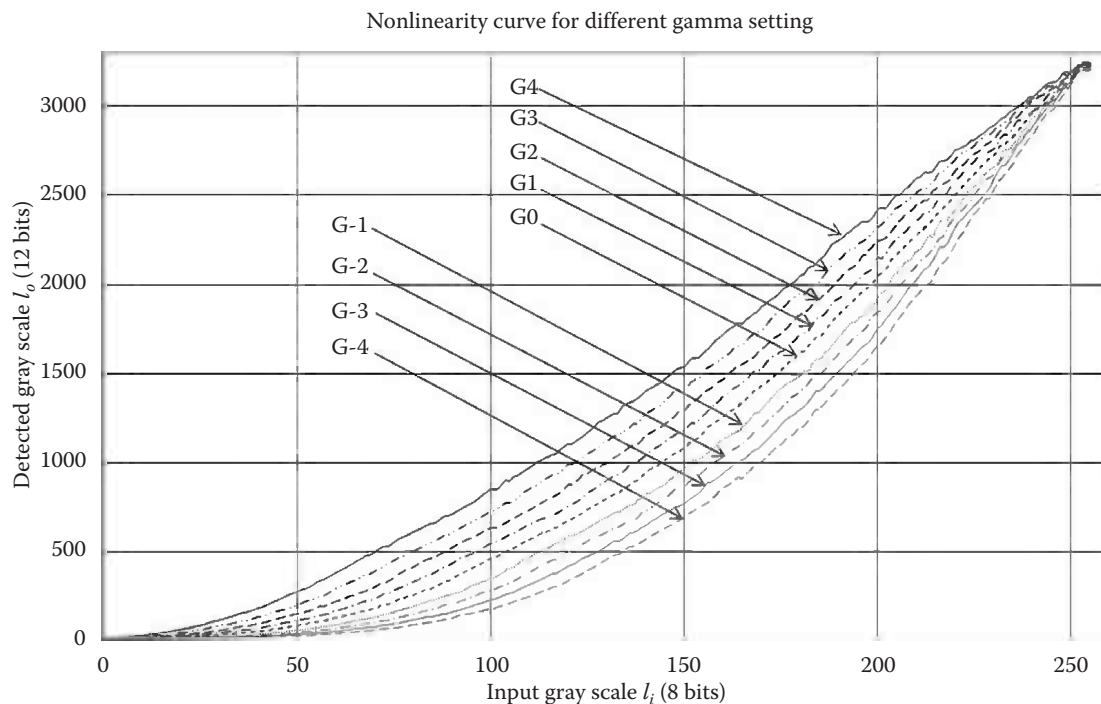


**FIGURE 7.22**  
Nonlinearity curves of a Canon SX50 LCOS projector.

### **7.5.1.3 Modeling and Calibration Error**

Selecting the correct modeling and calibration method is critical for accurate measurement. For a lens with large distortion (which may be a combination of magnification errors, field curvature, as well as geometric optical distortion), there is no way to obtain accurate results without correcting the lens errors using the calibration. Precision of the target, quality of the calibration setup, and calibration model including both selected intrinsic and extrinsic parameters all contribute to the calibration results.

The model used to convert an absolute phase map to a 3D point cloud is vital as well. For surfaces with curvatures, a simplified linear or partially linear model will result in very significant errors. In some cases that require multiview merging or extremely high accuracy, the light sheet from a grating or a digital projector cannot be taken as granted to be a flat plane. Instead, the light sheet has to be treated as a curved surface segment and needs to be fitted into a locally cylindrical surface.

### **7.5.1.4 Imbalance Error for Color Fringe Projections**

Color fringe patterns have been used for phase shifting because they provide unique features—they enable three  $120^\circ$  phase shifts in one color fringe, allowing for fast measurement in a vibrating environment. However, for color fringe projection,<sup>8,13,30,31,71</sup> color balance is a big challenge. Because the human eyes have different sensitivity to different colors, most digital projectors have different gamma settings for RGB colors. The color camera may also have a nonuniform spectral response. In phase-shifting measurement, any captured brightness variation due to these imbalances among the three channels (corresponding to three fringe images) may contribute to error and noises. Also, colorful object surface may be a problem and needs special considerations.<sup>76</sup>

### **7.5.1.5 Quantization Error**

Advancement in electronics has significantly reduced quantization error. Nowadays, 12 bits digital cameras are very common, which causes the digitization error to be in nanometer scale and thus negligible.<sup>74</sup> The digitization error in digital projectors can be reduced by use of a high-resolution projector with larger pitch and defocusing the projected fringes to act as a low-pass filter. Some projectors such as DLP can even accept 10 bits image input, which will reduce the digitization error significantly compared with the 8 bits data format.

### **7.5.1.6 Error and Noise from Environment**

It has been demonstrated using simulation that the phase error due to vibration and air turbulence has a frequency of two times the fringe spatial frequency.<sup>74</sup> An obvious option is to add vibration isolation or to shield the instrument. Other means of removing vibration noise include selecting an appropriate phase-shifting algorithm that is less sensitive to the vibration, capturing data faster with less images and shorter shutter time, and using simultaneous phase shifting or color fringes.

The background and electronic noise of the camera can be reduced by averaging several images for each fringe pattern. For digital projectors, a reasonably long camera shutter can let the fringe be more stable while too short of a shutter time may cause some problems because the camera may capture the image at the moment of either the refreshing

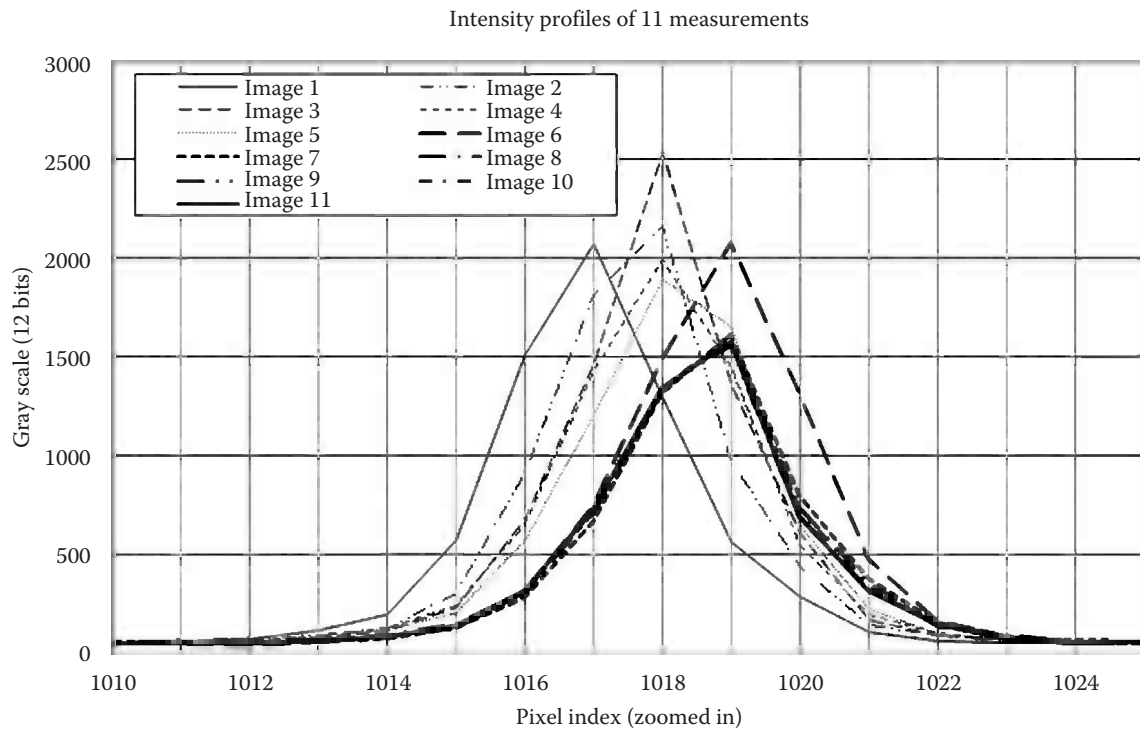


**FIGURE 7.23**  
Drift in a Canon SX50 LCOS digital projector.

transition from one image frame to another or the dynamic binary on/off integration of the projector chip pixels during image formation.

For highly accurate, repeatable, and reliable measurement, thermal drift may be another serious problem. For large FOV measurement, a 0.1 pixel drift may cause 0.5 mm coordinate displacement in the 3D space. Figure 7.23 shows drifts in a Canon SX50 LCOS projector. These projected line images were taken every 10 min, and the intensity profiles at the same cross section were drawn. As can be seen in the figure, severe drift exists.

### 7.5.2 Nonlinearity Compensation with the Projector Gamma $\gamma$

The linearity of the phase-shifting system is so important in obtaining high-accuracy, low-noise point cloud that many papers have been published in this area. This section discusses the two most widely used gamma correction techniques in digital phase-shifting systems.

#### 7.5.2.1 Gamma Correction with the Response Curve

As shown in Figure 7.22, nonlinearity in a digital projector can be very severe, and gamma correction is usually desirable. A first step is to pick up a gamma as close to linear as possible and then measure the system response to get a response curve like that in Figure 7.22. The response curve can be obtained by gradually changing the input gray level  $I_i$  and capturing the nonsaturated images with the fixed gamma setting and camera settings. A patch consisting of multiple pixels is used to reduce the noise by averaging their grayscale values as the response  $I_o$ .

One gamma correction method using the gamma curve is through a compensation function. A polynomial function up to ninth order is usually used to fit the gamma curve such as

$$I_i = a_0 + a_1 I_o + a_2 I_o^2 + a_3 I_o^3 + a_4 I_o^4 + a_5 I_o^5 + a_6 I_o^6 + a_7 I_o^7 + a_8 I_o^8 + a_9 I_o^9 \quad (7.84)$$

Every intensity value calculated in Equation 7.8 or 7.9 needs to be substituted into Equation 7.84 as  $I_o$  to calculate the required input  $I_i$  so that the output fringe profile via the projector is sinusoidal.

For the gamma  $\gamma=4$  curve in Figure 7.22, a noncompensated gamma response will project a nonsinusoidal fringe pattern, although the input to the projector is sinusoidal, as shown in Figure 7.24. After processing the gamma curve compensation, the 10 coefficients in Equation 7.84 are listed in Table 7.1.

The compensation process is demonstrated in Figure 7.25 using the compensation coefficients given in Table 7.1.

An alternative way to the compensation function is to use a lookup table (LUT) and interpolation to modify the calculated intensity by  $\Delta I$  from Equation 7.8 or 7.9 using

$$I' = I + \Delta I(I) \quad (7.85)$$

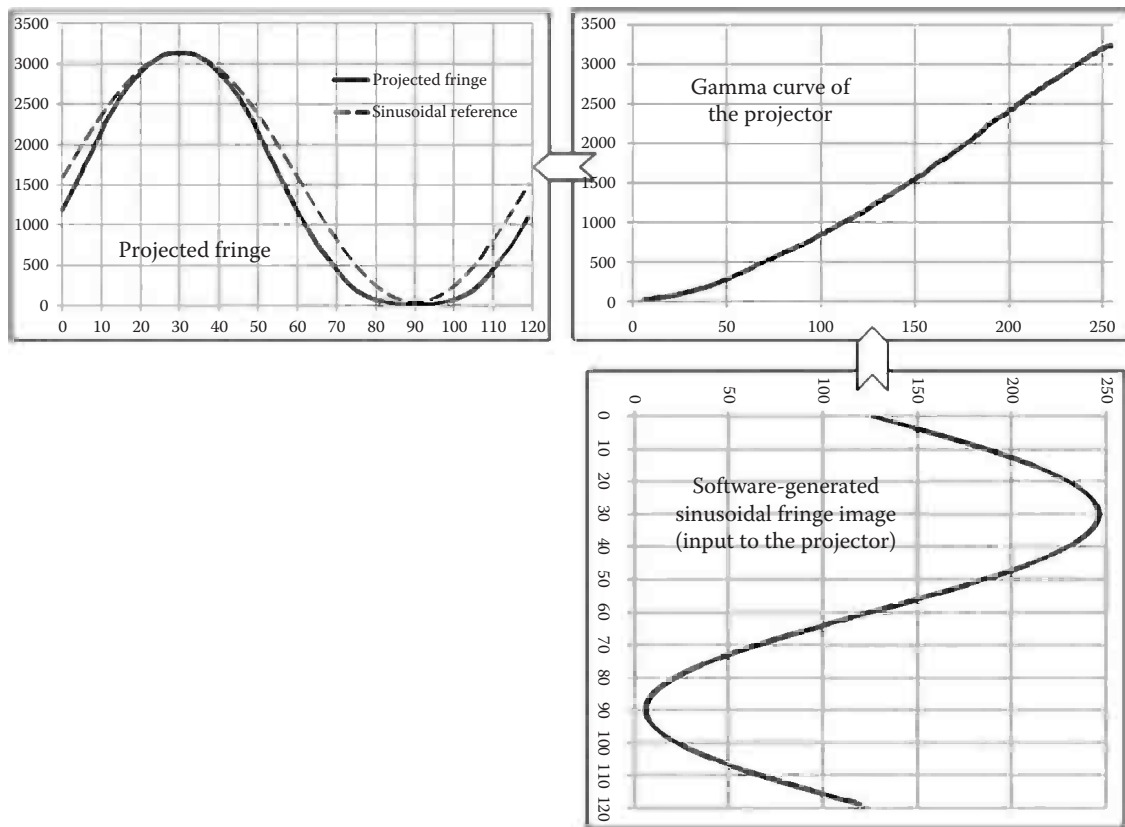


**FIGURE 7.24**

Projected fringe through a nonlinear projector (arrows indicate the data flow path).

**TABLE 7.1**  
Ten Compensation Coefficients

Coefficient $a_i$	Value
$a_0$	8.005962569868930e+00
$a_1$	3.767418142271050e+00
$a_2$	-1.417556486538000e-01
$a_3$	4.004162099686760e-03
$a_4$	-6.551477558101120e-05
$a_5$	6.464338860749370e-07
$a_6$	-3.910659971627370e-09
$a_7$	1.417609255380700e-11
$a_8$	-2.823177656665190e-14
$a_9$	2.372943262233540e-17

where  $\Delta I$  is a function of the calculated intensity  $I$  and is obtained by interpolating in the LUT.<sup>77</sup> The LUT is obtained by comparing the difference between the measured gamma curve and the ideal linear curve (upper curve), as shown in Figure 7.26. For each input grayscale value  $I$ , the system generates grayscale output  $g$ ; for the system to be linear, the required output grayscale should be  $g'$ , which needs input  $I'$ . In order to compensate for the nonlinearity, the calculated intensity  $I$  from Equation 7.8 has to be modified by  $\Delta I$ :

$$\Delta I = I' - I \quad (7.86)$$

The LUT is obtained by recording all calculated  $\Delta I$  for the input grayscale from 0 to 255 for 8 bits projector. Later when the fringe pattern is generated in the software using Equation 7.8, for each calculated  $I$ , the corresponding  $\Delta I$  has to be calculated from the LUT through internal interpolation and the input image to the projector is then calculated using Equation 7.85. Because interpolation is involved, this method requires the projector's gamma curve to be monotonic.

### 7.5.2.2 Gamma Correction with a One-Parameter Gamma Model

The use of a one-parameter gamma function to estimate both the phase and gamma is also a hot topic in addressing the nonlinearity problem.<sup>78-80</sup> The gamma function that describes the relationship between input  $I_i$  and output  $I_o$  with a gamma  $\gamma$  can be modeled as

$$I_o = I_i^\gamma \quad (7.87)$$

Estimating the phase value for a linear system from the calculated phase map under a non-linear system involves the phase shifting to obtain the phase and then an iterative process to estimate the gamma and phase alternatively. Some researchers also use the least-square fitting method with a few images to estimate the phase distribution<sup>79</sup> while others use many images for gamma estimation to apply a statistical method<sup>78</sup> or to reduce the error in gamma estimation.<sup>80</sup> Due to an error in the measurement and processing, the estimated gamma may vary from pixel to pixel in the image and the average of the estimated gamma over the entire image is taken as the "global" gamma. Using the gamma function (model)

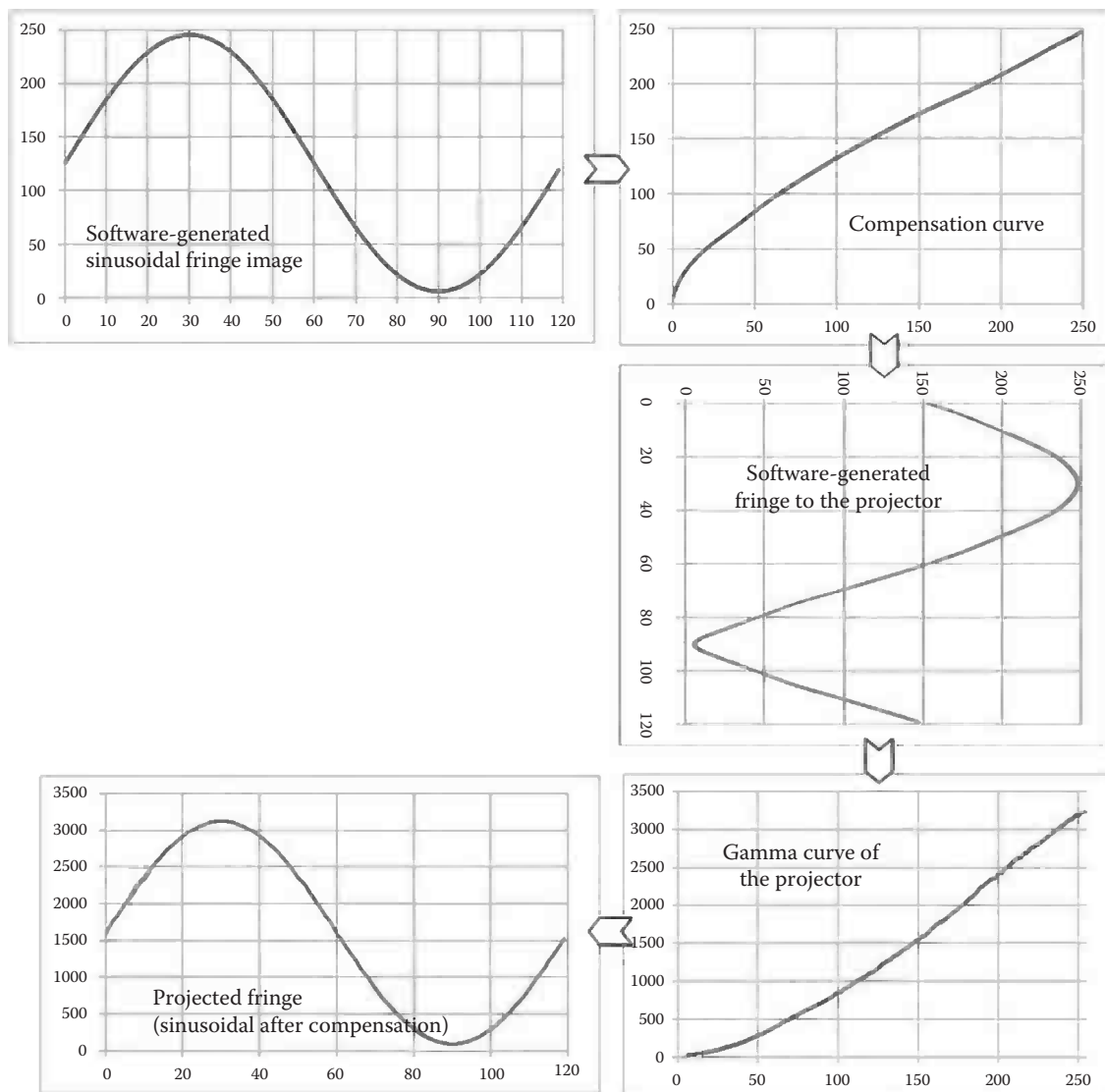


**FIGURE 7.25**  
Nonlinearity compensation process (arrows indicate the data flow path).

for phase estimation does not need the gamma curve and one-time compensation but it usually needs additional fitting or iteration, and thus is time consuming.

### 7.5.3 Phase Error Compensation

As an intermediate between the captured images and desired coordinates (point cloud), a phase map can also be compensated, a method that has some advantages. Compared with direct coordinate correction, phase compensation can be faster and easier to implement as long as a good correction mechanism can be built that is reliable and not dependent on the measurement settings during image capturing.

Over the past several years, such phase compensation techniques have started to emerge.<sup>77,81-83</sup> It has been demonstrated that the phase error due to the system nonlinearity

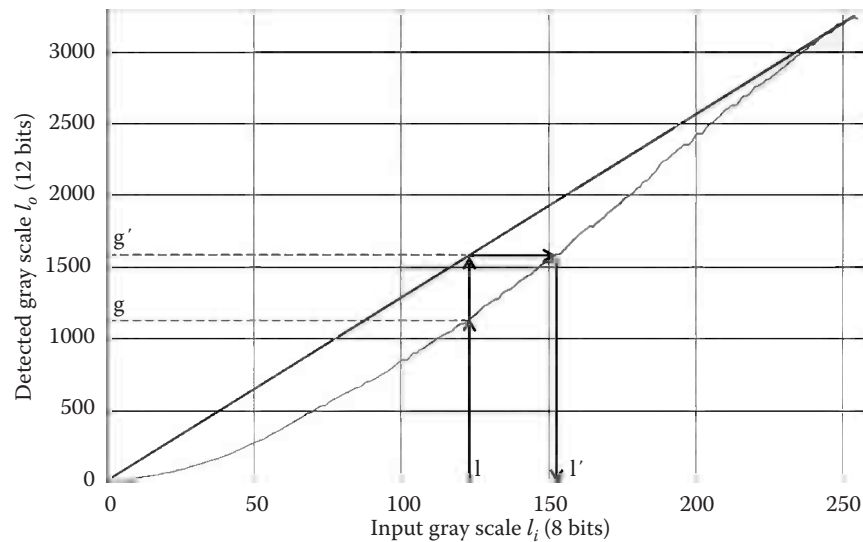


**FIGURE 7.26**  
Method for the LUT generation.

is independent of the pitch used in the fringe generation. The phase error LUT only needs to be built on one  $2\pi$  phase cycle. The required LUT is generated by performing a phase-shifting measurement with a large pitch on a white flat surface. The phase with and without nonlinearity issues is compared to construct the error map. The established phase error LUT can be applied to the wrapped phase map when a part is measured.

Some researchers<sup>84</sup> have also investigated the use of a phase compensation function to correct the distorted phase map directly through an inverse function. The inverse function is a polynomial function obtained through an iterative fitting process. After original phase shifting is performed, the calculated phase map is then modified by this correction function and the new phase map will have much less error from system nonlinearity.

Compared with the gamma correction discussed in the previous section, the phase error compensation technique takes more computing effort. The gamma correction can be done once before measurement while the phase correction has to be performed pixel by pixel after measurement.

#### 7.5.4 Coordinate Compensation

Although the effects of many error sources can be reduced by various means, the achieved accuracy may still be limited because there are some errors that cannot be reduced by these measures completely. This limitation makes direct coordinate error compensation a very important technique for measurement systems to reach higher accuracy without significantly increasing manufacturing cost.

##### 7.5.4.1 Coordinate Error Map

The first step for coordinate error compensation is to obtain an error map in the 3D space. This is performed by measuring a feature (point or surface) and comparing the measured data with a reference data point. Two methods were investigated to collect data for the

error map construction. One method is to use a flat surface as a reference. The measured data of the surface are fitted into a plane, and the deviation from the fitted plane at each point can be used as an error map at that location. Moving the target to various positions in the 3D space and obtaining the error map at each location provide an error map in the entire measurement volume.

The other method to obtain the error map is to use CMM to provide the coordinate reference.<sup>85</sup> In this setup, a small target with a dot in the center is mounted on a CMM probe. CMM moves the target to predetermined points in the measurement volume. At each point, the target is measured and the coordinates of its center dot are extracted. An error map in the 3D space can be obtained by comparing the measured coordinates with the CMM coordinates.

Once the error map is obtained, the errors in the measurement system can be compensated at measured points through either error functions or interpolation.

#### 7.5.4.2 Coordinate Error Compensation

In some cases, it is possible to find an error compensation function rather than use a LUT, especially when the system measurement volume and error map are symmetric, in which case the error functions are the easiest to reconstruct. A traditional method to reconstruct the error function  $\Delta$  is to fit the error map into a function of coordinates  $(x, y, z)$  and errors  $(e_x, e_y, e_z)$  such as

$$\Delta_x = f(x, y, z, e_x) \quad (7.88)$$

$$\Delta_y = f(x, y, z, e_y) \quad (7.89)$$

$$\Delta_z = f(x, y, z, e_z) \quad (7.90)$$

The coordinates  $(x', y', z')$  after compensation can be calculated as

$$(x', y', z') = (x + \Delta_x, y + \Delta_y, z + \Delta_z) \quad (7.91)$$

In general cases, the error map will not be symmetric, and it might be impractical to reconstruct an error function with high accuracy. More often, a LUT can be built to compensate the coordinate errors through interpolation. A 3D interpolation technique called Shepard's method<sup>86</sup> is used for error compensation in some research. The interpolated value  $s$  is given by a function

$$s(v) = \sum_{i=1}^N [w_i(v)\Delta(v_i)] \quad (7.92)$$

where

$v$  is a vector representing a point

$N$  is the number of points used in the interpolation

$\Delta(v_i)$  is the error at point  $v_i$

The weighting function  $w_i(v)$  has the form

$$w_i(v) = \frac{\|v - v_i\|^{-2}}{\sum_{j=1}^N \|v - v_j\|^{-2}} \quad (7.93)$$

Obviously, if  $v = v_i$ ,  $s(v) = \Delta(v_i)$ . If a point  $v_i$  is closer to the point  $v$  to be interpolated, it is given a larger weight. The Euclidean normal is defined as

$$\|v\| = \sqrt{\sum_{k=1}^K \xi_k^2} \quad (7.94)$$

where  $\xi_k$  is the element of vector  $v$ . In most cases,  $K=3$  and  $s$  can be the interpolated error in any coordinate direction depending on  $\Delta(v_i)$ . Since the error map is in the form of a 3D grid, the number of points used in the interpolation  $N$  can be set to be eight. For every measured point, the data set of the error map is searched to find the eight points that are the closest to the measured point and calculate their weight functions  $w_i(v)$  ( $i=1-8$ ) according to Equation 7.93. The interpolated error for the measured point is then calculated by Equation 7.92. This error is then subtracted from the measured coordinates of the point to improve measurement accuracy.

---

## 7.6 Summary

In this chapter, we tried to detail the science and methods behind the field of phase shifting-based methods. These methods have been used in a wide range of commercial systems made for such applications as reverse engineering of part geometry, process control of formed parts like airfoil and sheet metal structures, as well as small area mapping of features like edge breaks on machined part out to dental impressions of people's teeth. The use of phase-shifting methods has been made more widely practical by high-speed computers and larger memory chips that allow a typical phase-shift measurement to be made in a few seconds in most cases and at the frame rates of cameras using some dedicated hardware.

In Chapter 1, we discussed some of the challenges in applying 3D technology for industrial metrology purposes. In subsequent chapters, we will present a wide range of examples of applications of this technology.

---

## References

1. E. Hetcht, *Optics*, 3rd edn., Addison-Wesley, Reading, MA (1998).
2. M. S. Mermelstein, D. L. Feldkhun, and L. G. Shirley, Video-rate surface profiling with acousto-optic accordion fringe interferometry, *Optical Engineering*, 39, 106 (2000); doi: 10.1117/1.602342.
3. H. Takasaki, Moiré topography, *Applied Optics*, 9(6), 1467–1472 (1970).

4. F. P. Chiang, Moiré methods for contouring, displacement, deflection, slope and curvature, *Proceedings of SPIE*, 153, 113–119 (1978).
5. Y. Wang, and P. Hassell, Measurement of thermally induced warpage of BGA packages/substrates using phase-stepping shadow moiré, *Proceedings of the First Electronic Packaging Technology Conference*, Singapore, pp. 283–289 (1997).
6. K. G. Harding and S. L. Cartwright, Phase grating use in moiré interferometry, *Applied Optics*, 23(10), 1517 (1984).
7. K. Creath and J. C. Wyant, Moiré and fringe projection techniques, in *Optical Shop Testing*, D. Malakara (ed.), 3rd edn., Chapter 16, pp. 559–652 John Wiley & Sons, New York (2007).
8. P. S. Huang, Q. Hu, F. Jin, and F.-P. Chiang, Color-encoded digital fringe projection technique for high-speed three-dimensional surface contouring, *Optical Engineering*, 38, 1065 (1999); doi: 10.1117/1.602151.
9. P. S. Huang, F. Jin, and F.-P. Chiang, Quantitative evaluation of corrosion by a digital fringe projection technique, *Optics and Lasers in Engineering*, 31(5), 371–380 (1999).
10. Y. Y. Hung, L. Lin, H. M. Shang, and B. G. Park, Practical three-dimensional computer vision techniques for full-field surface measurement, *Optical Engineering*, 39, 143–149 (2000).
11. P. S. Huang, S. Zhang, and F.-P. Chiang, Trapezoidal phase-shifting method for three-dimensional shape measurement, *Optical Engineering*, 44, 123601 (2006).
12. L. C. Chen, X. L. Nguyen, and Y. S. Shu, High speed 3-D surface profilometry employing trapezoidal HSI phase shifting method with multi-band calibration for colour surface reconstruction, *Measurement Science and Technology*, 21(10), 105309 (2010).
13. S. Lina, Y. Shuang, and W. Haibin, 3D measurement technology based on color trapezoidal phase-shifting coding light, *IEEE 9th International Conference on the Properties and Applications of Dielectric Materials* (ICPADM 2009), Harbin, China, pp. 1094–1097 (2009).
14. L. Chen, C. Quan, C. J. Tay, and Y. Fu, Shape measurement using one frame projected sawtooth fringe pattern, *Optics Communications*, 246(4–6), 275–284 (2005).
15. K. Creath, Phase-measurement interferometry techniques, in *Progress in Optics*, Vol. 26, Chapter 5, Elsevier Science Publishers B.V., Amsterdam, the Netherlands (1988).
16. M. Kujawinska, Use of phase-stepping automatic fringe analysis in moiré interferometry, *Applied Optics*, 26(22), 4712–4714 (1987).
17. H. Schreiber and J. H. Bruning, Phase shifting interferometry, in *Optical Shop Testing*, 3rd edn., John Wiley & Sons, New York, pp. 547–655 (2007).
18. D. C. Ghiglia and M. D. Pritt, *Two-Dimensional Phase Unwrapping: Theory, Algorithms, and Software*, 1st edn., John Wiley & Sons, New York (1998).
19. Q. Hu and K. G. Harding, Conversion from phase map to coordinate: Comparison among spatial carrier, Fourier transform, and phase shifting methods, *Optics and Lasers in Engineering*, 45, 342–348 (2007).
20. Q. J. Hu, Modeling, error analysis, and compensation in phase-shifting surface profilers, *Proceedings of SPIE*, 8133, 81330L (2011).
21. Q. Hu, K. G. Harding, X. Du, and D. Hamilton, Shiny parts measurement using color separation, *Proceedings of SPIE*, 6000, 60000D (2005).
22. C. Ai and J. C. Wyant, Effect of piezoelectric transducer nonlinearity on phase shift interferometry, *Applied Optics* 26(6), 1112–1116 (1987).
23. M. P. Kothiyal and C. Delisle, Polarization component phase shifters in phase shifting interferometry: Error analysis, *Optica Acta: International Journal of Optics*, 33(6), 787–793 (1986).
24. Y.-B. Choi and S.-W. Kim, Phase-shifting grating projection moiré topography, *Optical Engineering*, 37(3), 1005–1010 (1998).
25. J. Y. Cheng and Q. Chen, An ultrafast phase modulator for 3D imaging, sensors, cameras, and systems for scientific/industrial applications VII, in *IS&T Electronic Imaging*, *Proceedings of SPIE*, Vol. 6068, M. M. Blouke (ed.), 60680L (2006).
26. B. F. Oreb, I. C. C. Larkin, P. Fairman, and M. Chaffari, Moiré based optical surface profiler for the minting industry, in *Interferometry: Surface Characterization and Testing*, *Proceedings of SPIE*, Vol. 1776 (1992).

27. J. Pan, R. Curry, N. Hubble, and D. A. Zwemer, Comparing techniques for temperature-dependent warpage measurement, *Global SMT & Packaging*, 14–18 (February 2008).
28. A. J. Boehnlein and K. G. Harding, Field shift moire, a new technique for absolute range measurement, *Proceedings of SPIE*, 1163, 2–13 (1989).
29. L. H. Bieman, K. G. Harding, and A. Boehnlein, Absolute measurement using field shifted Moiré, in *Optics, Illumination, and Image Sensing for Machine Vision VI, Proceedings of SPIE*, Vol. 1614, pp. 259–264 (1991).
30. K. G. Harding, M. P. Coletta, and C. H. VanDommelen, Color encoded Moiré contouring, in *Optics, Illumination, and Image Sensing for Machine Vision III, D. Svetkoff (ed.), Proceedings of SPIE*, Vol. 1005, pp. 169–178 (1988).
31. M.-S. Jeong and S.-W. Kim, Color grating projection moiré with time-integral fringe capturing for high-speed 3-D imaging, *Optical Engineering*, 41(8), 1912–1917 (2002).
32. P. S. Huang, C. Zhang, and F.-P. Chiang, High-speed 3-D shape measurement based on digital fringe projection, *Optical Engineering*, 42, 163 (2003).
33. S. Zhang and P. S. Huang, High-resolution, real-time three-dimensional shape measurement, *Optical Engineering*, 45(12), 123601 (2006).
34. C. L. Koliopoulos, Simultaneous phase shift interferometer, in *Advanced Optical Manufacturing and Testing II, Proceedings of SPIE*, Vol. 1531, V. J. Doherty (ed.) pp. 119–127 (1992).
35. J. C. Wyant, Advances in interferometric metrology, in *Optical Design and Testing, Proceedings of SPIE*, Vol. 4927, pp. 154–162 (2002).
36. L.-C. Chen, S.-L. Yeh, A. M. Tapilouw, and J.-C. Chang, 3-D surface profilometry using simultaneous phase-shifting interferometry, *Optics Communications*, 283(18), 3376–3382 (2010).
37. D. W. Phillion, General methods for generating phase-shifting interferometry algorithm, *Applied Optics*, 36(31), 8098–8115 (1997).
38. Q. Hu, P. S. Huang, Q. Fu, and F. P. Chiang, Calibration of a three-dimensional shape measurement system, *Optical Engineering*, 42, 487 (2003).
39. P. S. Huang, Q. Hu, and F. P. Chiang, Double three-step phase-shifting algorithm, *Applied Optics*, 41(22), 4503–4509 (2002).
40. P. S. Huang and H. Guo, Phase shifting shadow moiré using the Carré algorithm, in *Two- and Three-Dimensional Methods for Inspection and Metrology VI, Proceedings of SPIE*, 7066, 70660B (2008).
41. Q. Kemaoy, S. Fangjun, and W. Xiaoping, Determination of the best phase step of the Carré algorithm in phase shifting interferometry, *Measurement Science and Technology*, 11, 1220–1223 (2000).
42. P. Hariharan, B. F. Oreb, and T. Eiju, Digital phase-shifting interferometer: A simple error-compensating phase calculation algorithm, *Applied Optics*, 26, 2504–2506 (1987).
43. K. G. Larkin, Efficient nonlinear algorithm for envelope detection in white light interferometry, *Journal of the Optical Society of America A*, 13(4), 832–843 (1996).
44. J. Novak, Five-step phase-shifting algorithms with unknown values of phase shift, *Optik-International Journal for Light and Electron Optics*, 114(2), 63–68 (2003).
45. H. Zhang, M. J. Lalor, and D. R. Burton, Robust, accurate seven-sample phase-shifting algorithm insensitive to nonlinear phase-shift error and second-harmonic distortion: A comparative study, *Optical Engineering*, 38, 1524 (1999).
46. K. Hibino, B. F. Oreb, D. I. Farrant, and K. G. Larkin, Phase-shifting algorithms for nonlinear and spatially nonuniform phase shifts, *Journal of the Optical Society of America A*, 14(4), 918–930 (1997).
47. K. G. Larkin and B. F. Oreb, A new seven-sample symmetrical phase-shifting algorithm, in *SPIE Conference on Interferometry Techniques and Analysis, SPIE Proceedings*, Vol. 1755, San Diego, CA pp. 2–11 (1992).
48. K. H. Womack, Interferometric phase measurement using spatial synchronous detection, *Optical Engineering*, 23, 391–395 (1984).
49. M. Kujawinska, Spatial phase measurement methods, in *Interferogram Analysis: Digital Fringe Pattern Measurement Techniques*, D. W. Robinson and G. T. Reid (eds.), Institute of Physics, Bristol, U.K. pp. 141–193 (1993).

50. J. Xu, Q. Xu, and H. Peng, Spatial carrier phase-shifting algorithm based on least-squares iteration, *Applied Optics*, 47, 5446–5453 (2008).
51. W. Osten, P. Andrae, W. Nadeborn, and W. Jijptner, Modern approaches for absolute phase measurement, *Proceedings of SPIE*, Vol. 2647, *International Conference on Holography and Correlation Optics*, O. V. Angelsky (ed.), Chernovtsy, Ukraine, pp. 529–540 (1995).
52. H. Cui, W. Liao, N. Dai, and X. Cheng, A flexible phase-shifting method with absolute phase marker retrieval, *Measurement*, 45(1), 101–108 (2012).
53. K. Creath, *Phase-Measuring Interferometry Techniques [Progress in Optics XXVII]*, Elsevier Science Publishers B.V., Amsterdam, the Netherlands, pp. 349–393 (1988).
54. L. Tao, K. Harding, M. Jia, and G. Song, Calibration and image enhancement algorithm of portable structured light 3D gauge system for improving accuracy, in *Optical Metrology and Inspection for Industrial Applications, Proceedings of SPIE*, Vol. 7855, 78550Y-1, K. Harding, P. S. Huang, and T. Yoshizawa (eds.), 78550Y (2010).
55. Y. Wang and P. Hassell, Measurement of the thermal deformation of BGA using phase-shifting shadow Moiré, *Electronic/Numerical Mechanics in Electronic Packaging*, 2, 32–39 (1998).
56. J. Pan, R. Curry, N. Hubble, and D. Zwemer, *Comparing Techniques for Temperature Dependent Warpage Measurement*. Plus 10/2007, pp. 1–6.
57. G. Mauvoisin, F. Brémand, and A. Lagarde, Three-dimensional shape reconstruction by phase-shifting shadow Moiré, *Applied Optics*, 33(11), 2163–2169 (1994).
58. Q. Hu, K. G. Harding, D. Hamilton, and J. Flint, Multiple views merging from different cameras in fringe-projection based phase-shifting method, *Proceedings of SPIE* 6762, 676207 (2007).
59. Q. Hu, P. S. Huang, and F. P. Chiang, 360-degree shape measurement for reverse engineering, *Proceedings of the International Conference on Flexible Automation and Intelligent Manufacturing (FAIM 2000)*, University of Maryland, College Park, MD (June 2000).
60. R. Y. Tsai, A versatile camera calibration technique for high-accuracy 3-D machine vision metrology using off-the-shelf TV cameras and lenses, *IEEE Journal of Robotics and Automation*, RA-3(4), 323–344 (1987).
61. Z. Zhang, A flexible new technique for camera calibration, Microsoft Research Technical Report MSR-TR-98-71.
62. A. M. McIvor, Nonlinear calibration of a laser stripe profiler, *Optical Engineering*, 41(01), 205–212 (2002).
63. S. Zhang, and P. Huang, Novel method for structured light system calibration, *Optical Engineering*, 45(08), 083601 (2006).
64. J. Heikkilä and O. Silvén, A four-step camera calibration procedure with implicit image correction, *IEEE Proceedings of the 1997 Conference on Computer Vision and Pattern Recognition (CVPR '97)*, San Juan, PR, pp. 1106–1112 (1997).
65. R. Legarda-Sáenz, T. Bothe, and W. P. Jüptner, Accurate procedure for the calibration of a structured light system, *Optical Engineering*, 43(2), 464–471 (2004).
66. S. Q. Jin, L. Q. Fan, Q. Y. Liu and R. S. Lu, Novel calibration and lens distortion correction of 3D reconstruction systems, *International Symposium on Instrumentation Science and Technology, Journal of Physics: Conference Series*, 48, 359–363 (2006).
67. K. M. Dawson-Howe and D. Vernon, Simple pinhole camera calibration, *International Journal of Imaging Systems and Technology*, 5(1), 1–6 (1994).
68. J. Kannala and S. S. Brandt, A generic camera model and calibration method for conventional, wide-angle and fish-eye lenses, *IEEE Transactions on Pattern Analysis and Machine Intelligence*, 28(8), 1335–1340 (2006).
69. T. Rahman and N. Krouglicof, An efficient camera calibration technique offering robustness and accuracy over a wide range of lens distortion, *IEEE Transactions on Image Processing*, 21(2), 626–637 (2012).
70. Y. Yin, X. Peng, Y. Guan, X. Liu, A. Li, Calibration target reconstruction for 3-D vision inspection system of large-scale engineering objects, in *Optical Metrology and Inspection for Industrial Applications, Proceedings of SPIE*, Vol. 7855, K. Harding, P. S. Huang, and T. Yoshizawa (eds.), Beijing, China, 78550V (2010).

71. C. Sinlapeecheewa and K. Takamasu, 3D profile measurement by color pattern projection and system calibration, *IEEE International Conference on Industrial Technology (IEEE ICIT'02)*, Bangkok, Thailand, Vol. 1, pp. 405–410 (2002).
72. T. S. Shen and C. H. Menq, Digital projector calibration for 3-D active vision systems, *Journal of Manufacturing Science and Engineering*, 124(2), 126–134 (2002).
73. M. Kimura, M. Mochimaru, and T. Kanade. Projector calibration using arbitrary planes and calibrated camera. *2007 IEEE Computer Society Conference on Computer Vision and Pattern Recognition (CVPR 2007)*, IEEE Computer Society, Minneapolis, MN, June 18–23 (2007).
74. K. Creath, Error sources in phase measuring interferometry, *Proceedings of SPIE*, Vol. 1720, *International Symposium on Optical Fabrication, Testing, and Surface Evaluation*, J. Tsujiuchi (ed.), Tokyo, Japan, pp. 428–435 (1992).
75. K. Creath and J. Schmit, Errors in spatial phase-stepping techniques, *Proceedings of SPIE*, Vol. 2340, *Interferometry '94: New Techniques and Analysis in Optical Measurements*, M. Kujawinska and K. Patorski (eds.), Warsa, Poland, pp. 170–176 (1994).
76. L. C. Chen et al., High-speed 3D surface profilometry employing trapezoidal phase-shifting method with multi-band calibration for colour surface reconstruction, *Measurement Science and Technology*, 21(10), 105309 (2010).
77. S. Zhang and P. S. Huang, Phase error compensation for a 3-D shape measurement system based on the phase-shifting method, *Optical Engineering*, 46, 063601 (2007); doi: 10.1117/1.2746814.
78. H. Guo, H. He, and M. Chen, Gamma correction for digital fringe projection profilometry, *Applied Optics*, 43, 2906–2914 (2004).
79. T. M. Hoang, Simple gamma correction for fringe projection profilometry system, *SIGGRAPH 2010*, Los Angeles, CA, July 25–29 (2010).
80. K. Liu, Y. Wang, D. L. Lau, Q. Hao, and L. G. Hassebrook, Gamma model and its analysis for phase measuring profilometry, *Journal of the Optical Society of America A*, 27(3), 553–562 (2010).
81. S. Zhang and S.-T. Yau, Generic nonsinusoidal phase error correction for three-dimensional shape measurement using a digital video projector, *Applied Optics*, 46(1), 36–43 (2007).
82. H. Cui, X. Cheng, N. Dai, T. Yuan, and W. Liao, A new phase error compensate method Of 3-D shape measurement system using DMD projector, *Fourth International Symposium on Precision Mechanical Measurements, Proceedings of SPIE*, Xinjiang, China, 7130, 713041 (2008).
83. X. Chen, J. Xi, and Y. Jin, Phase error compensation method using smoothing spline approximation for a three-dimensional shape measurement system based on gray-code and phase-shift light projection, *Optical Engineering*, 47, 113601 (2008).
84. Y. Liu, J. Xi, Y. Yu, and J. Chicharo, Phase error correction based on inverse function shift estimation in phase shifting profilometry using a digital video projector, in *Optical Metrology and Inspection for Industrial Applications, Proceedings of SPIE*, 7855, K. Harding, P. S. Huang, and T. Yoshizawa (eds.), 78550W (2010).
85. P. S. Huang, Q. Hu, and F. P. Chiang, Error compensation for a three-dimensional shape measurement system, *Optical Engineering*, 42, 482 (2003).
86. P. Alfeld, Scattered data interpolation in three or more variables, in *Mathematical Methods in Computer Aided Geometric Design*, T. Lyche and L. Schumaker (eds.), Academic Press, Boston, MA, pp. 1–33 (1989).